IN-SITU INSTRUMENTATION FOR DEGRADATION MONITORING OF POWER SEMICONDUCTOR DEVICES IN POWER ELECTRONICS CONVERTERS

by

Chondon Roy

A dissertation submitted to the faculty of
The University of North Carolina at Charlotte
in partial fulfillment of the requirements
for the degree of Doctor of Philosophy in
Electrical Engineering

Charlotte

2023

Approved by:

Dr. Babak Parkhideh

Dr. Badrul Chowdhury

Dr. Robert Cox

Dr. Xiuli He

ABSTRACT

CHONDON ROY. In-situ instrumentation for degradation monitoring of power semiconductor devices in power electronics converters. (Under the direction of DR. BABAK PARKHIDEH)

Modern power and energy systems rely heavily on power electronics converters. The most significant component of these converters is the power semiconductor switching devices MOSFETs/IGBTs. Two critical parameters that provide real-time information about the stress and aging of these devices are the junction temperature (T_j) and On-state resistance (R_{DSON}) of the MOSFETs. By actively controlling and modeling these parameters, it is possible to increase the converter's useful lifetime and predict failure. Additionally, if real-time stress information is available, it is possible to balance stress among multiple converters by balancing converter operating conditions. Power semiconductor devices such as MOSFETs/IGBTs degrade through different degradation mechanisms in long-term applications. Failure of MOSFETs/IGBTs is one of the primary causes of power electronics failure. The R_{DSON} and T_j of a MOSFET are key health-indicating parameters. This dissertation presents sensing circuit designs that enable real-time monitoring of the oR_{DSON} and T_j of the MOSFETs/(IGBTs). The sensing circuits are integrated into a three-phase 1000 VDC to 480 VAC DC-AC inverter for a complete online in-situ health monitoring system of the MOSFETs. A new on-state drain-source voltage (V_{DSON}) sensing circuit has been used to monitor the R_{DSON} of the high-side MOSFETs. This sensor references the drain of the high-side transistors for their V_{DSON} measurement and allows V_{DSON} measurement of multiple high-side transistors with respect to the same ground reference. The high-side V_{DSON} measurement circuits combined with low-side V_{DSON} measurement circuits have been used for a complete R_{DSON} monitoring of all the MOSFETs in the inverter. The drain current (I_{DS}) is captured from measurements using an off-the-shelf current sensor located at the output filter inductor. Account-

ing for propagation delays in the measurement circuitry, both the V_{DSON} and I_{DS} are sampled and converted into digital data multiple times in a switching cycle, filtered, and stored in a digital signal processor (DSP). The DSP, originally used for the inverter control, then processes the sensor data captured over one grid cycle and calculates the average R_{DSON} of the MOSFETs of the inverter. Validations of all the sensing circuits, using theoretical analysis and hardware experiments along with the software implementation for data processing and handling are presented in the dissertation for this real-time, in-situ R_{DSON} measurement. Furthermore, a method of mapping the MOSFET's R_{DSON} to the T_j for real-time accurate T_j estimation of the MOSFETs.

DEDICATION

I dedicate this thesis to my parents, who have always been my guiding light and source of inspiration. Their unwavering support and encouragement have been instrumental in helping me achieve this milestone in my life.

ACKNOWLEDGEMENTS

I would like to express my sincere gratitude to my supervisor, Dr. Babak Parkhideh, for his invaluable guidance and support throughout my research. I am deeply grateful for his mentorship and the opportunities he provided me.

I would also like to thank the committee members Dr. Badrul Chowdhury, Dr. Robert Cox, and Dr. Xiuli He for their valuable feedback on my dissertation. Their insights and suggestions helped me improve the quality of my work.

I am grateful to the Department of Electrical and Computer Engineering and the Energy Production and Infrastructure Center (EPIC) at Charlotte for providing the necessary coursework, lessons, and lab facilities for my graduate study and this research. I would also like to acknowledge the financial support received from the ECE department, EPIC, and the graduate school throughout my graduate study.

I would like to thank my lab mates and colleagues at Charlotte Dr. Namwon Kim, Mr. Hossein Niakan, Mr. Zaheen Mustakin, Mr. Ali Parsa Sirat, Dr. Daniel Evans, Mr. Andrew LeClair, and Mr. James Gafford for their collaboration on various research projects. Their contributions were invaluable to the success of this research.

I am also grateful to my closest friends Dr. Abdullah-Al-Raihan Nayeem, Dr. ABM Mohaimenur Rahman (Bivor), Fatema-E-Jannat (Putul), Jannatul Ferdous (Moon) who were a family for me in the United States. Their support made my life way easier and I can not thank them enough for their unconditional support.

Finally, I would like to express my heartfelt gratitude to my parents, my brother, and my sister for their unwavering support and encouragement throughout my academic journey. It is they who helped me come this far from a small village in Bangladesh and I am forever indebted to them.

TABLE OF CONTENTS

LIST OF TABLES

LIST OF FIGURES

LIST OF ABBREVIATIONS

AC Alternating current.

ADC Analog to digital conversion.

DC Direct current.

DMM Digital multi-meter.

DPT Double pulse test.

DSP Digital signal processor.

DUT Device under test.

EMI Electromagnetic interference.

HB Half-bridge.

HEMT High electR_{ON} mobility transistor.

I_{DS} Drain-source current.

IGBT Insulated gate bipolar transistor.

MOSFET Metal oxide field effect transistor.

PWM Pulse width modulation.

R_{DSON} On-state drain-source resistance.

R_{ON} On-state resistance.

SiC Silicon carbide.

T_c Case temperature.

T_j Junction temperature.

V_{CEON} On-state collector-emitter voltage.

V_{DSON} On-state drain-source voltage.

V_D Diode forward voltage drop.

V_{ON} On-state voltage.

CHAPTER 1: INTRODUCTION

1.1 Motivation

Power electronics converters are an essential part of our modern electrical system. An estimated 70% of the total electric energy undergoes through power electronics converters from generation to end-users [1], which will eventually be 100% in the near future due to more and more use of power electronics in the modern energy system. From consumer electronics devices such as cellphones, computers, etc. to commercial electric vehicles, almost all modern machinery requires power electronics converters to condition and supply power to different components. The use of Wide bandgap (WBG) semiconductor devices in power electronics is adding more fuel to the use of power electronics in the energy system, which is reflected in the development of more and more power electronics courses and teaching materials [2, 3]. Figure 1.1 presents an example of electric energy flow from generation to end-users.

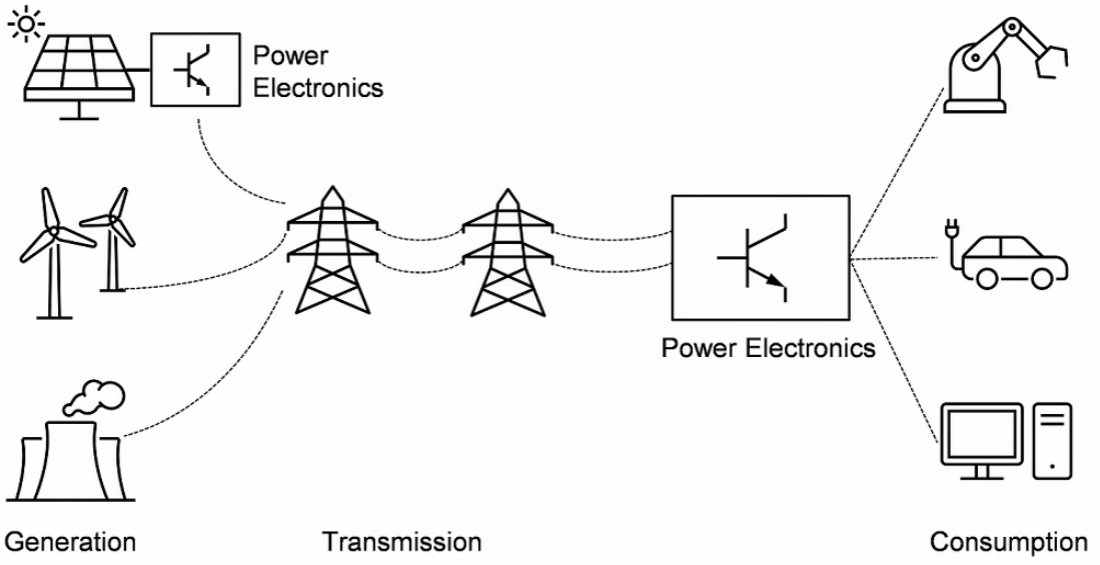

Figure 1.1: Electrical energy flow from generation to end-users.

However, power electronics converters are prone to failure. According to a recent survey [4] on dc-dc converters conducted among different industries and academia, 15% converters frequently fail, 60% converters fail occasionally and only 25% converters rarely fail during their lifetime.

Among many different components in the power converters, 57.1% of the converter failures are attributable to the power semiconductors failures [4], 23.8% failures to the resonant capacitor tank, and the remaining failures are due to failures in the other components of the converters. Figure 1.2 shows the failure rate among the DC-DC converters in the survey [4] and a breakdown of the different causes of the converter failure.

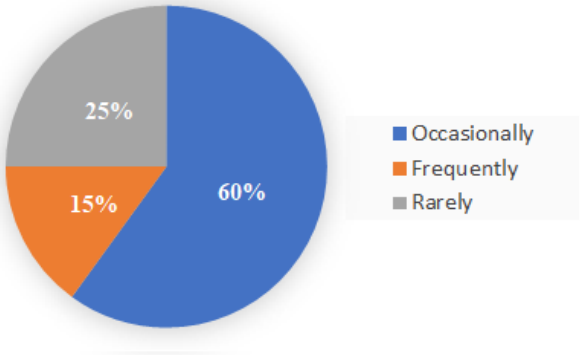

(a) Failure rate of DC-DC converters.

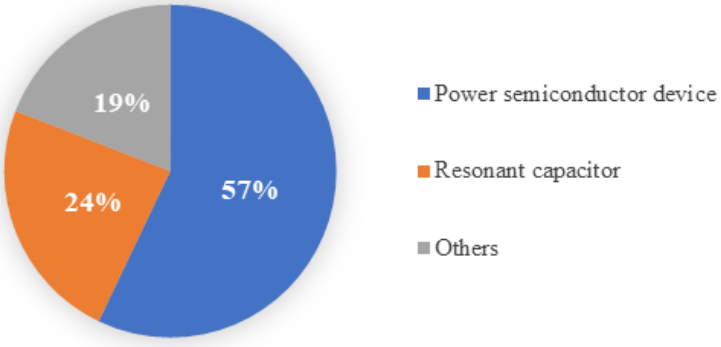

(b) Different contributor to the failures of failed DC-DC converters.

Figure 1.2: DC-DC converter failure rates and different failure contributors to the failure according to a recent survey [4] among industries and academia.

As power semiconductor devices are one of the primary causes of converter failures, the reliability of a power electronics converter can be improved by improving the reliability of the power semiconductor devices. The reliability of the power semiconductor devices can be improved by properly monitoring the device's health and taking necessary actions to prevent sudden failure. This dissertation focuses on finding a reliable method to monitor the health of the power semiconductor devices and the implementation of an online in-situ health monitoring architecture in a practical power electronics converter built using Silicon Carbide (SiC) Metal Oxide Field Effect Transistors (MOSFET).

1.2 Literature Review

In recent years, there have been many researches on real-time monitoring of power semiconductor devices to increase reliability and prevent potential failure. The power semiconductor (MOSFETs/IGBTs/HEMTs) devices ages through different degradation mechanisms caused by various electro-mechanical stresses in long-term operations. Under long-term operational stresses, degradation in different parts of the power semiconductor device results in reduced performance and potential failure. Different methods of detection of device degradation are discussed in recent research articles published in major power electronics transactions and conferences. The aging of the devices causes a shift in different electrical parameters that can be measured using intelligent sensing mechanisms. Reference [5, 6, 7, 8, 9, 10, 11, 12, 13, 14, 15, 16, 17, 18, 19, 20, 21, 22, 23, 24, 25, 26, 27, 28, 29, 30, 31, 32] present power semiconductor health monitoring method using on-state drain-source voltage (V_{DSON}) of SiC/ Si MOSFETs or on-state collector-emitter (V_{CEON}) of IGBTs as the health indicating parameter. Reference [10, 12, 19, 30, 31, 33, 34, 35] present methods, circuits, and justification of monitoring turn-on threshold voltage as the health indicating parameter. Research [24, 36, 37] considers the turn-on Miller plateau as the degradation parameter. [38, 39, 40, 41] presents device health monitoring using gate current of the

MOSFETs. MOSFET/IGBT junction temperature and case temperature are utilized as a degradation monitoring method in [19, 27, 42, 43, 44, 45, 46]. Several other electrical parameters, such as short circuit current, switching transient measurements, body diode forward voltage drop, etc., can also be utilized as the health monitoring indicator [10, 29, 40, 47, 48, 49, 50, 51, 52, 53, 54, 55, 56, 57, 58, 59, 60].

Figure 1.3 presents a summary of the electrical parameters considered for device health monitoring of the recently published articles reviewed in this dissertation.

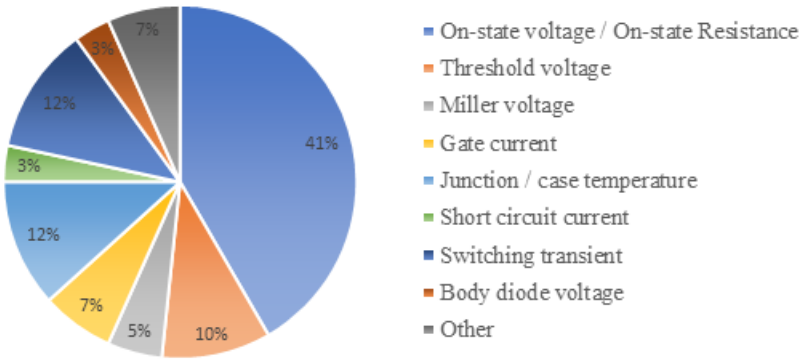

Figure 1.3: Survey on health indicating parameters for MOSFETs/IGBTs in recently published articles.

Although there have been many research works on the health monitoring of power semiconductor devices to enhance the reliability of power electronics converter, most of the research is limited to a single device tests circuit such as a Double Pulse Test (DPT) setup or a single device converter such as a buck converter. Only a few research focuses on the health monitoring of the power semiconductor devices in a system-level application [18, 21, 25, 29]. Reference [21, 25] present online health monitoring of the IGBT modules in a three-phase inverter. The method uses an external current source to inject a predefined current into the IGBT modules to measure the V_{CEON} of the modules and compares that with the baseline values to estimate device health. In this architecture, only one sensing circuit has been used and a selector switch is used to select specific IGBT modules for health monitoring. This method can not monitor the

health of the IGBT during regular operation of the inverter due to the requirement of external current injection. Reference [18, 29] present online health monitoring of MOSFETs/ IGBTs in a three-phase inverter using system-level signals. In this approach, the system-level circuit measures the summation of the on-state voltage (V_{ON}) of one device and the forward diode voltage drop (VD) of a complementary device in another leg. While this method simplifies the circuit design, it does not provide independent component-level data. Independent and simultaneous V_{CEON}/ V_{DSON} measurement of individual transistors is more effective as a failure of a single transistor may lead to the failure of the entire system.

1.3 Proposed Solutions

1.3.1 Online in-situ R_{DSON} monitoring

The focus of this dissertation is the implementation of a complete online in-situ R_{DSON} monitoring of all power transistors (MOSFETs) used in a practical three-phase DC-AC inverter containing multiple half-bridge (HB) legs. To the best of the author's knowledge, no prior work implementing a complete online R_{DSON} monitoring of an inverter has been published at the time of preparing this manuscript. This dissertation addresses the challenges of the simultaneous R_{DSON} monitoring of all MOSFETs during real-time inverter operations and proposes the implementing solution. The contributions of the online in-situ R_{DSON} monitoring can be divided into three major areas:

1. Developing efficient sensing circuitry for the in-situ and online measurement of the V_{DSON} of the MOSFETs in a multi-phase converter configuration. Different methods of V_{DSON} sensing circuits have been reviewed, and a new on-state drain-source voltage V_{DSON} sensing circuit allowing a common reference of the analog measurement signals for all high-side MOSFETs is proposed. The proposed circuit can be configured in different ways for application-specific mea-

surement solutions. The proposed solution reduces the number of components by reducing the number of isolated power supplies and the total number of sensing signals. Reduction of the number of components and the number of sensing signals results in simplified computation stress and reduced size and weight of the overall system. The proposed solution is also minimally invasive and can be installed over existing inverter hardware with little design upgrade.

2. Implementation of online in-situ monitoring of V_{DSON}/R_{DSON} in a 75 kW three-phase inverter containing three silicon carbide (SiC) MOSFET HB modules. An in-situ V_{DSON} measurement board is designed to measure the independent V_{DSON} of all the six SiC MOSFETs and this board is installed on pre-designed inverter hardware without altering the hardware assembly. The hardware design, mechanical and electrical interconnection connection, and experimental validation are presented in this manuscript.

3. Data sampling, synchronizing, qualifying, and computing strategies are developed to obtain meaningful R_{DSON} data out of a noisy environment during the inverter operation. The proposed signal processing strategy is essential to minimize the impact of electromagnetic interference (EMI) noises generated by the sinusoidal switching operation of six MOSFET devices in a three-phase inverter.

1.3.2 Junction temperature monitoring using online R_{DSON} measurement

The junction temperature of MOSFETs/IGBTs is a vital indicator of the device's health. In most cases, MOSFETs fail due to overheating. There could be different underlying reasons for the overheating. Therefore real-time knowledge of the device's junction temperature can help prevent sudden device failure. This dissertation presents a test procedure to create a mapping between the device R_{DSON} and junction temperature. The mapping can be used to monitor the real-time junction temperature of the MOSFET from the R_{DSON} measurement. The real-time junction temperature

can be used in active control [61, 62, 63]. Dynamic control, such as re-distributing power among parallel converters, changing the output power, and changing other operating conditions, can keep the T_j within the device's safe operating range to increase useful lifetime.

1.4 Organization of Dissertation

This dissertation is organized as follows: Chapter 2 presents the challenges and solutions of online in-situ R_{DSON} monitoring. Chapter 3 presents different methods to measure V_{DSON} with circuit analysis and experimental validation. Chapter 4 presents the implementation of a complete online in-situ R_{DSON} monitoring in a 75 kW DC-AC inverter and junction temperature mapping with the R_{DSON}. Chapter 5 presents the conclusions and future work.

CHAPTER 2: ONLINE IN-SITU R_{DSON} MONITORING CHALLENGES AND SOLUTIONS

An online health monitoring system requires two primary components, sensors that obtain necessary data and a control system that processes the sensor data. The concept of online in-situ R_{DSON} monitoring is to extract and record the R_{DSON} during real-time converter operation with sensors and processors within the converter. In the in-situ R_{DSON} measurement, V_{DSON} and drain-source current (I_{DS}) measurements of power transistors need to be sent to the control system to calculate the R_{DSON}. However, in a multi-phase converter with multiple HB legs, all V_{DSON} measurements of individual power transistors do not have a common V_{DSON} measurement reference. Therefore, different devices' measured V_{DSON} cannot be directly tied to the control reference. This issue challenges implementing the in-situ prognostics to practical power electronic converters. V_{DSON} of individual transistors can be measured using the voltage clamping circuits [13, 64, 65, 23, 18], where the source of the individual device is the reference of the measurement. The challenge is translating these measurements to the control system's ground reference. In a multi-phase inverter, the lack of a common signal reference for the transistors increases the complexity of V_{DSON} measurement. Each V_{DSON} sensor requires a separate isolated power supply, resulting in a high system cost. Therefore, an advanced V_{DSON} measurement system is designed to have a common reference of measurements for the high-side transistors by the authors [66]. This design allows all the high-side V_{DSON} measurement sensors to be powered using a single isolated power supply in the proposed circuit. This work uses the V_{DSON} measurement system to obtain online R_{DSON}.

Furthermore, when multiple switching devices are involved, their sinusoidal switching pattern generates EMI that requires special attention in analog and digital signal processing. The EMI generated from all devices affects the measured signals at different electrical nodes, and the measured signals contain unpredictable signal noises. Therefore, the analog data sampling strategy becomes essential to extract meaningful data from analog measurements.

These challenges remain unaddressed in the experimental research involving only one switching device but are addressed in this dissertation. Another challenge is the validation of the experiment results. No off-the-shelf V_{DSON}/R_{DSON} sensors are readily available to compare the experimental results except with the datasheet provided numbers. The R_{DSON} provided in a standard MOSFET datasheet is a range of a large number of MOSFETs. For example, the CAS300M17BM2 [67] datasheet lists $8 - 10m\Omega$ R_{DSON} for 300 A current at room temperature. It is important to know the actual R_{DSON} of the DUT to validate the in-situ measurement circuits. The maximum R_{DSON} is 25% higher than the typical value listed, which is a large number to evaluate the in-situ measurement accuracy. Therefore, for an accurate comparison, each of the six MOSFETs used in the inverter is characterized under controlled pre-set conditions to have the baseline measurements, which have been used later for comparison with the in-situ measurements.

CHAPTER 3: V_{DSON} SENSING CIRCUIT DESIGN AND CONFIGURATION

The voltage across a power MOSFET is usually hundreds of volts when the MOSFET is in the off state and in millivolts when the MOSFET is in the on-state. A V_{DSON} sensing circuit needs to measure the on-state voltage with high precision. To enable a high precision measurement, the V_{DSON} sensing circuit utilizes a voltage clipping and clamping mechanism to block the off-state high voltage. It only measures the on-state low amplitude voltage signal. Figure 3.1 presented a simplified block diagram of the conventional (left) and proposed modified (right) V_{DSON} sensor architecture. Conventionally, the V_{DSON} measurement circuit ground is connected to the MOSFET's source or lower potential node. The proposed V_{DSON} measurement circuit utilizes the higher potential node or the drain of the MOSFET as the ground reference of the measurement and conditioning circuit. The combination of these two variants of the V_{DSON} sensing circuits enables us to deploy different architectures based on different applications.

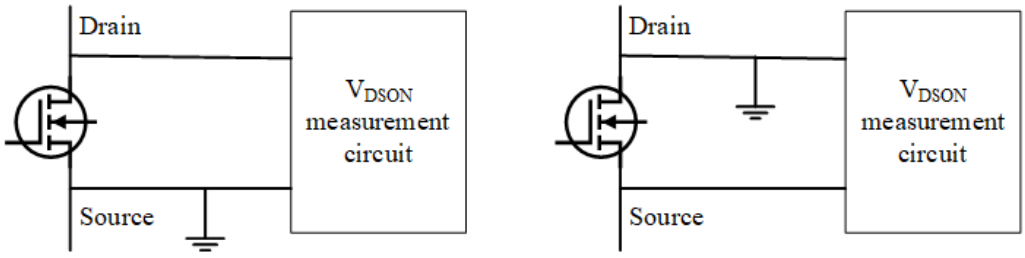

Figure 3.1: Simplified block diagram of the V_{DSON} sensor. The figure on the left is conventionally used where the ground is connected to the source terminal of the MOSFET. And the modified V_{DSON} sensor is on the right, where the ground is connected to the drain of the MOSFET

Two possible combinations are discussed in this dissertation, and one of them is used for the online in-situ health monitoring of a three-phase inverter. Figure 3.2 shows the two possible configurations. The configuration on the left use a drain-referenced V_{DSON} sensor for the high-side MOSFET and a source-referenced V_{DSON} sensor for the low-side MOSFET. The configuration on the right uses a drain-referenced V_{DSON} sensor for the low-side MOSFET and a source-referenced V_{DSON} sensor for the high-side MOSFET. As the drain of the low-side MOSFET and the source of the high-side MOSFET in an HB is the same node, this configuration has a single ground reference for both the high and low-side MOSFETs.

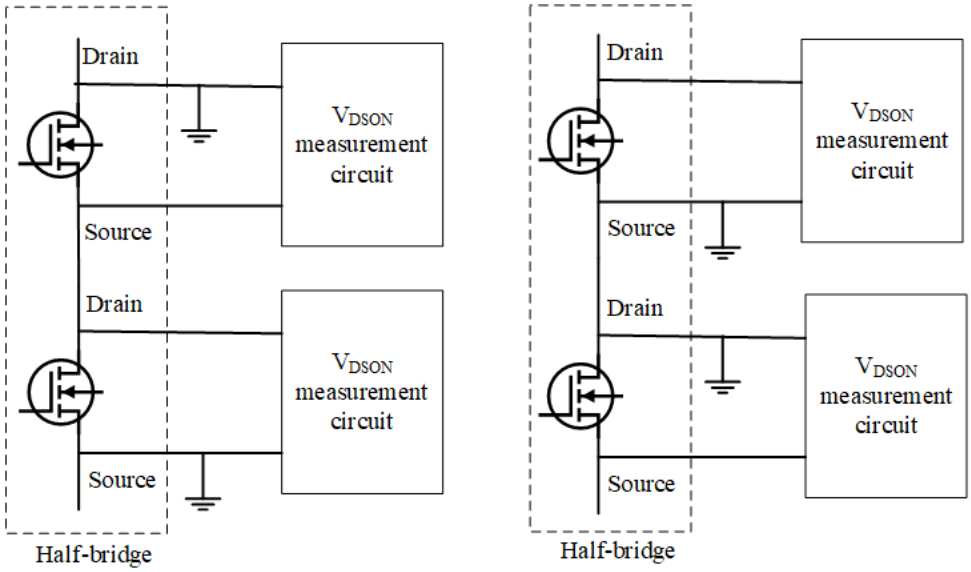

Figure 3.2: Simplified block diagram of two V_{DSON} sensor configurations in a half-bridge. The figure on the left presents a high-side low-side tied configuration where the high-side and low-side V_{DSON} sensor reference grounds are different. And the figure on the right presents a center-point tied configuration where the measurement reference ground is the same node for both the high-side and low-side MOSFETs

3.1 High-side and low-side tied configuration

3.1.1 Circuit analysis

In this configuration all the high-side V_{DSON} sensing circuit reference to the same measurement ground, which is the DC bus positive terminal. On the other hand, the low-side V_{DSON} sensing circuits reference to the DC bus negative terminal. Figure 3.3 presents an example of this configuration in a three-phase DC-AC inverter. This configuration allows having the same measurement reference for all the high-side devices and another measurement reference for the low-side devices. Having the same measurement reference simplifies the circuit design and requires only one isolated power supply for all the high-side V_{DSON} sensors and another for all the low-side V_{DSON} sensors. Thus this configuration reduces the number of power supplies to two from six for a three-phase DC-AC inverter.

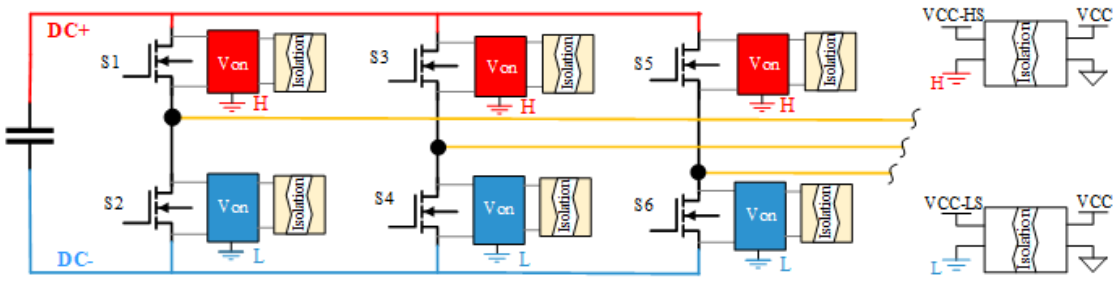

Figure 3.3: High-side and low-side bus tied V_{DSON} sensor configuration.

Figure 3.4 presents the detailed schematics of the high-side and low-side V_{DSON} measurement circuits in a half-bridge for the high-side, low-side tied configuration. The proposed drain-referenced V_{DSON} measurement circuit measures the V_{DSON} of the high-side transistors in reference to the drain (DC Bus +), as opposed to referencing to the source terminal that is used in conventional V_{DSON} measurement circuits. Different nodes in the circuit are marked as nodes 1, 2, 3, and 4. Figure 3.5 presents the ideal waveforms at different nodes. The V_{DSON} measurement circuit has three stages. The first stage is clamping, which clamps the high voltage when the transistor

is off and passes only the low V_{DSON} when the transistor is on. A high-voltage Schottky diode (D1) is connected to the source of the high-side transistor, which only allows current flow from the source to the V_{DSON} measurement circuit. The V_{DSON} measurement circuit references the drain of the high-side transistor. The clamped point indicated as node 1, where the cathode of the blocking diode (D1) is connected, has a voltage potential within a setpoint set by the Zener diode (DZ1) (3V in the circuits used in this research) below the drain potential. When the transistor is turned off, it has a much higher potential in its drain terminal than the source. Therefore, the blocking diode (D1) becomes reverse-biased and disconnects the source terminal from the measurement circuit. When the transistor is turned on, the transistor has a very small potential difference between the drain and the source terminals. This potential difference makes the blocking diode (D1) forward-biased, completing the circuit through the transistor. Node 1 now measures the inverted sum of V_{DSON} and the forward voltage drop (VF) of the Schottky diode (D1); this is listed in Table 3.1.

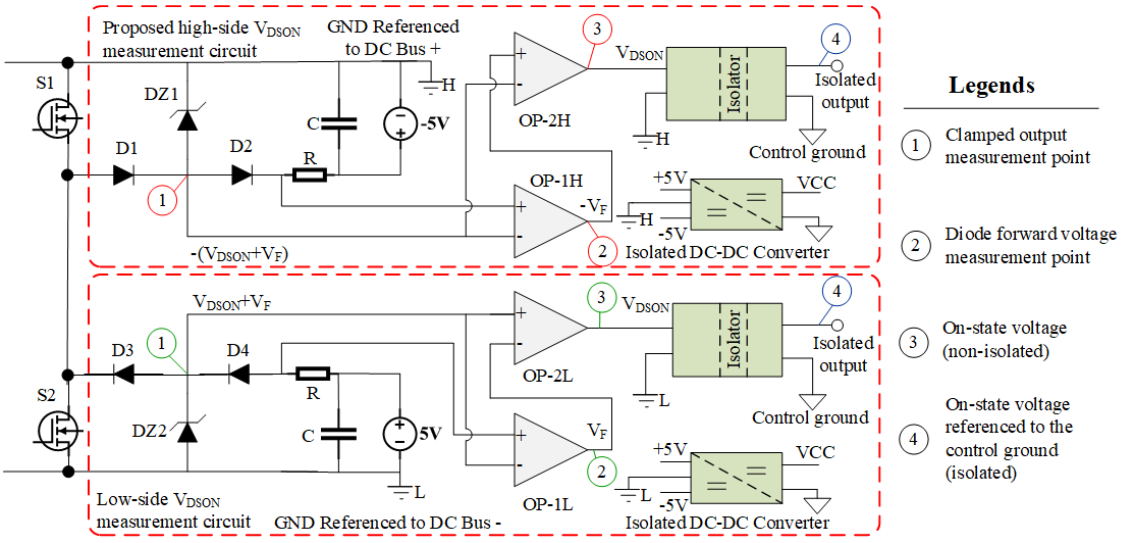

Figure 3.4: The proposed circuit for high-side and low-side V_{DSON} measurement. The nodes circled red are referenced to DC+, the nodes circled green are referenced to DC- and the nodes circled blue are referenced to the control ground. The same circuit is repeated for the three phases, except the same power supplies are used for all three phases.

Actual V_{DSON} can be calculated by subtracting the diode forward voltage drop (VF) from the absolute value of the voltage at node 1. However, the Schottky diode's forward voltage drop depends on the current through it and the junction temperature. Estimating the forward voltage drop across the Schottky diode is possible if the temperature is known; however, accurate and reliable junction temperature estimation is problematic. To overcome this issue, another Schottky diode (D2), the same as the blocking diode (D1), is placed in series very close to the blocking diode (D1) so that they operate at a similar temperature level. When the transistor is on, the same current flows through these two diodes (D1 and D2), ensuring the same forward voltage drop across each of these two diodes. The voltage drop across the second diode (D2) is measured using a differential amplifier circuit which is a part of the second stage of the V_{DSON} measurement circuit. The output of this circuit is measured at node 2. The voltage at node 1 is then subtracted from the voltage at node 2 to get the V_{DSON} of the DUT indicated at node 3. Node 4 is the last stage output that translates the measured V_{DSON} from the measurement circuit reference (DC Bus +) to the control circuit reference.

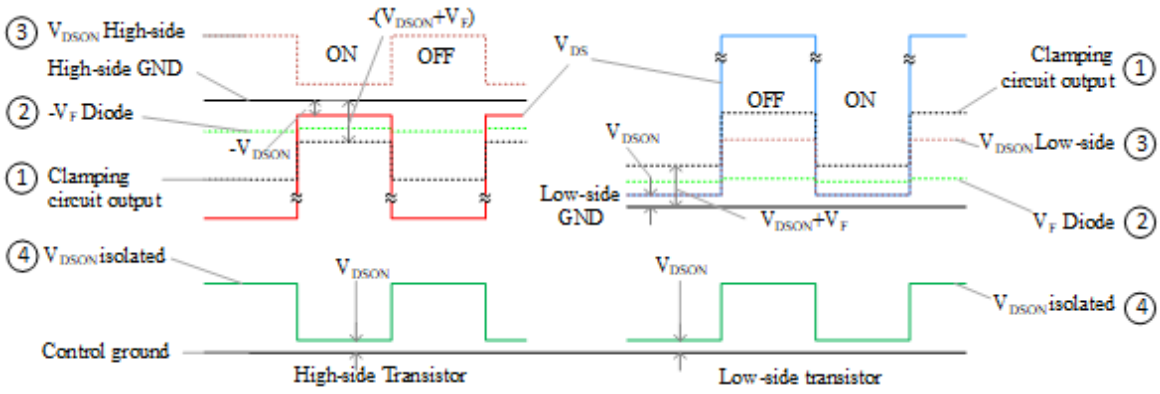

Figure 3.5: Ideal waveform of the proposed V_{DSON} monitoring circuit, high-side (left) and low-side (right).

The low-side V_{DSON} measurement circuit works similarly, except it references the negative DC bus (DC Bus -). Table 3.1 describes the voltages at different measure-

ment nodes.

Table 3.1: V_{DSON} circuit operation and measurement at different nodes.

Node	MOSFET status	High-side	Low-side
1	ON	-(V_{DSON}+V_F)	V_{DSON}+V_F
1	OFF	-3V	3V
2	X	-V_F	V_F
3	ON	V_{NODE2}-V_{NODE1} =V_{DSON}	V_{NODE1}-V_{NODE2} =V_{DSON}
3	OFF	V_{NODE2}-V_{NODE1}=3-V_F	V_{NODE1}-V_{NODE2}=3-V_F

3.1.2 Sensor board and experiment results

Figure 3.6 presents a photograph of the developed printed circuit board containing 8 V_{DSON} sensors for 8 MOSFETs in four legs in a three-phase DC-AC inverter using the CREE SiC HB modules [67].

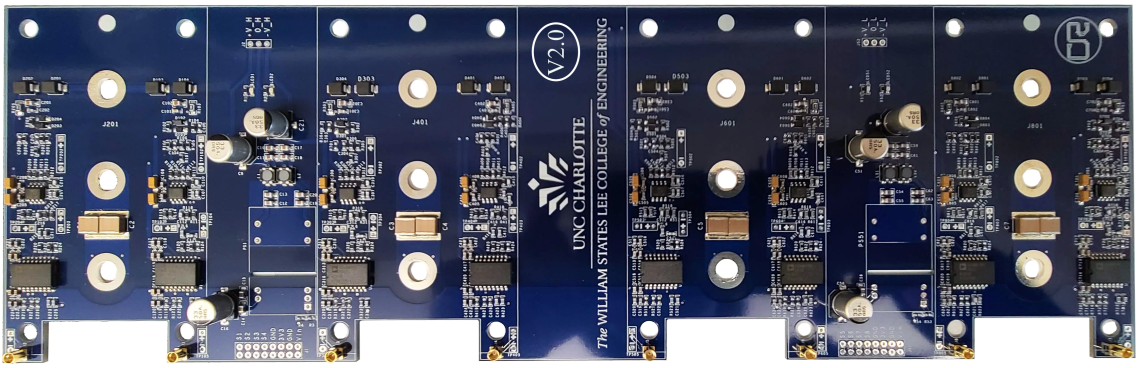

Figure 3.6: Developed V_{DSON} sensor board for a three-phase four leg DC-AC inverter.

Both the high-side and low-side V_{DSON} sensing circuits have been tested under static and dynamic operating conditions. To verify the performance of the conditioning circuits a DPT is conducted and measured signals at different nodes are compared with the theoretical analysis and ideal waveforms. Figure 3.7 presents the measured signals for the high-side V_{DSON} sensor and figure 3.8 presents the measured signals

for the low-side V_{DSON} sensor.

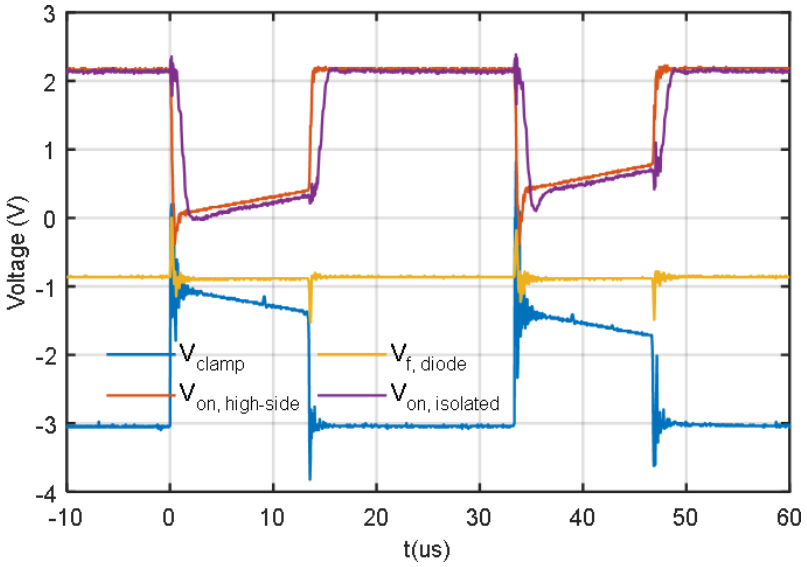

Figure 3.7: Experiment results on different nodes for the high-side V_{DSON} sensor.

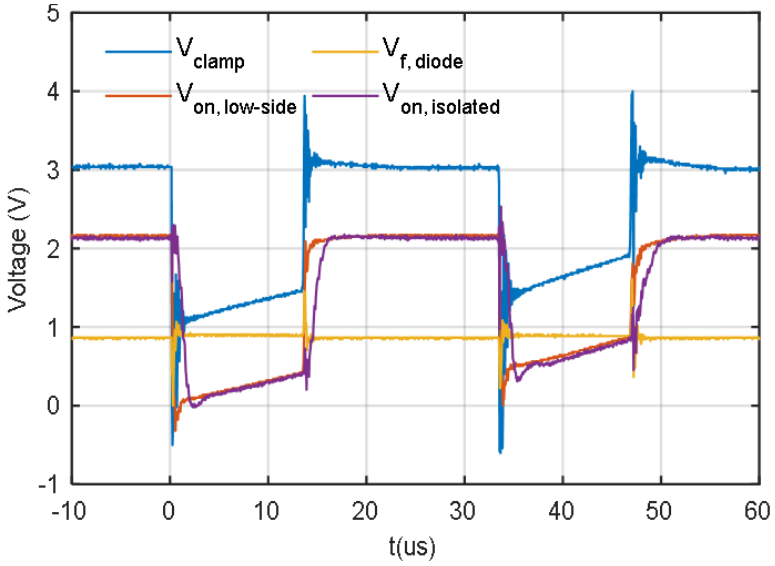

Figure 3.8: Experiment results on different nodes for the low-side V_{DSON} sensor.

Figure 3.9 presents the final output of the high-side V_{DSON} sensor isolated output with the device drain current in a DPT. The measured signal is translated into the proper units and presented in figure 3.10. The translated signals are then used to calculate the R_{DSON} of the device under test (DUT). The calculated R_{DSON} is presented in figure 3.11. Cree CAS300M17BM2 [67] modules are used as the DUT and

based on the datasheet the R_{DSON} of this MOSFET ranges from 6-8 $m\Omega$. And the calculated R_{DSON} in the DPT is around 7 $m\Omega$. Therefor the V_{DSON} sensing circuit operation is validated. The low-side V_{DSON} sensor outputs also match the datasheet provided R_{DSON} of the MOSFET. Figure 3.12 presents the calcualted R_{DSON} during the second pulse of the DPT for all the six MOSFETs.

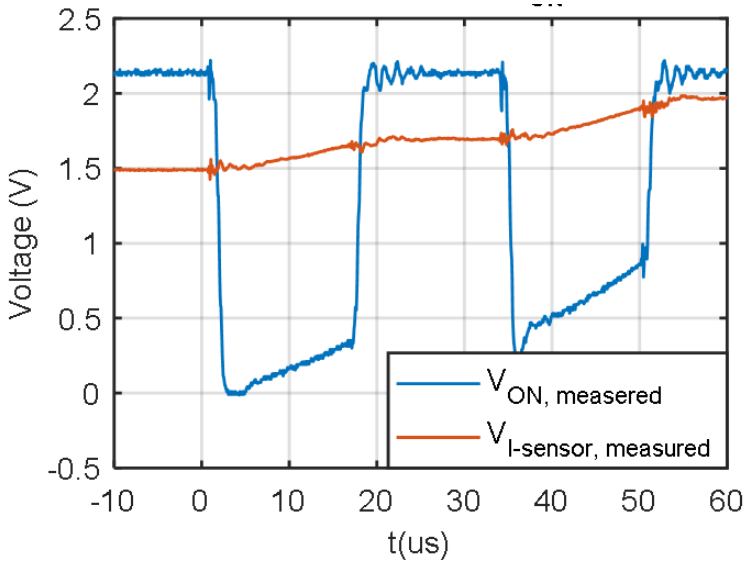

Figure 3.9: Final output of the high-side V_{DSON} sensor and device drain current under DPT.

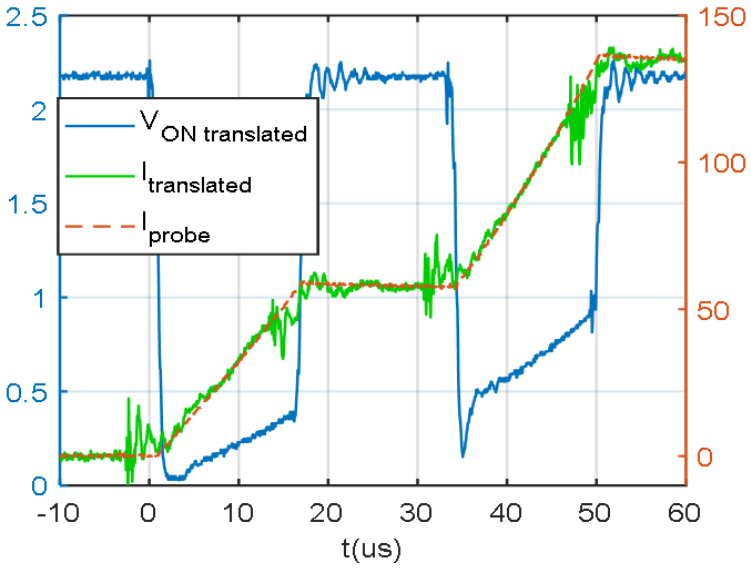

Figure 3.10: Final outputs of the high-side V_{DSON} sensor and device drain current translated into proper units.

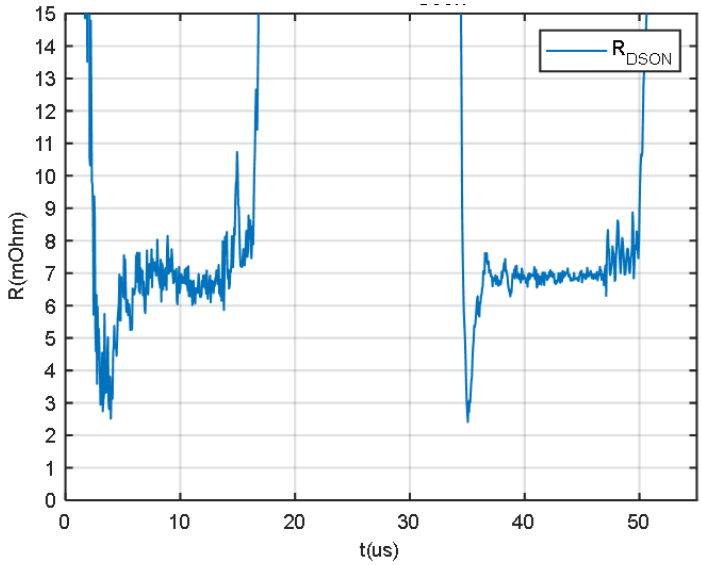

Figure 3.11: Calculated R_{DSON} of the high-side MOSFET using the measured sensor data.

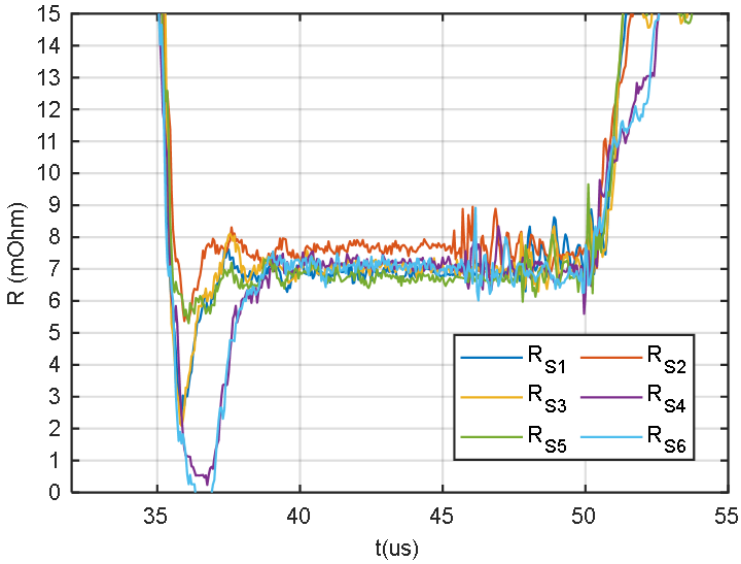

Figure 3.12: Measured R_{DSON} of the six MOSFETs in three half-bridge legs of the three-phase inverter.

3.2 Center-point tied half-bridge V_{DSON} sensor configuration

In most applications, the high-side and low-side devices in an HB are turned ON and OFF in a complimentary manner. When the high-side device is turned ON, the low-side device is turned OFF, and vice versa to prevent shoot-through. The

proposed (HBV_{DSON}) sensor [68] measures the V_{DSON} of both the high-side and low-side devices independently and then combines them into a single sensor output. Figure 3.13 presents the block diagram of the proposed HBV_{DSON} sensor connected to the three terminals of an HB leg consisting of two MOSFETs.

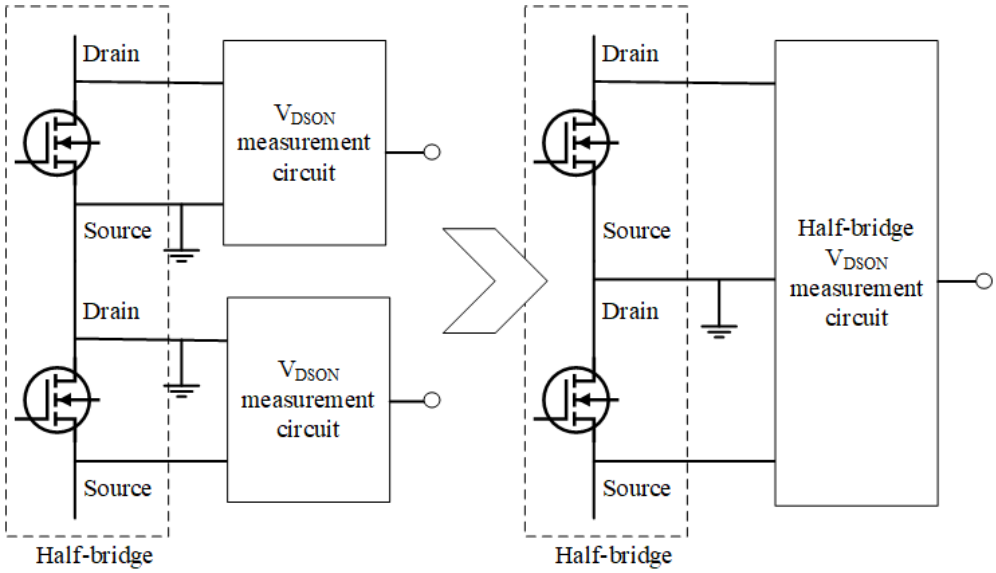

Figure 3.13: Block diagram of the half-bridge V_{DSON} measurement signal. This configuration combines two output signals of the high-side and low-side MOSFETs into one measurement signal.

3.2.1 Circuit analysis

Figure 3.14 presents the detailed schematics block diagram of the HBV_{DSON} sensor. The HBV_{DSON} sensor consists of two independent sensing circuits for the low-side and high-side devices. The fundamental operating principle of the individual sensing circuits is presented in [66]. The HBV_{DSON} sensor consists of four circuit stages. The novelty of the HBV_{ON} sensor is the combination of the high-side and low-side circuits by swapping their orientation. In the configuration discussed in the previous section, the high-side V_{DSON} sensor references DC+, and the low-side V_{DSON} sensor references DC-. But in the HBV_{ON} both the high-side and low-side V_{DSON} sensors reference the middle point of a half-bridge and eventually, the outputs of two V_{DSON} sensors are combined to have one single sensor output. The HBV_{DSON} sensor consists of six

major signal processing stages.

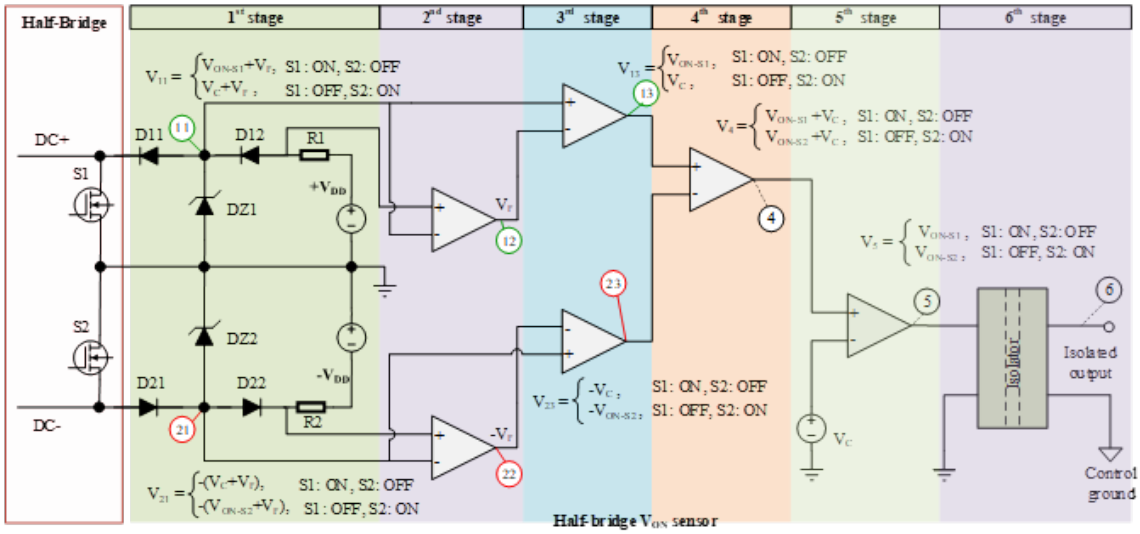

Figure 3.14: Schematic diagram of the half-bridge V_{DSON} measurement sensor. The final output of the sensor contains V_{DSON} information of both the high-side and low-side MOSFETs.

The first stage is the clamping circuit that clamps the high voltages from the transistor nodes when the transistors are in off-state. The components (except the blocking diodes) used in the sensor has lower voltage rating (under 25V) while the HB operates in hundreds of volts. The blocking diodes block the high-voltage and clamp the sensing circuit voltages within a set voltage to prevent damage to the circuit. The operating principle of the combined voltage clamping circuits is highlighted in Figure 3.15 When the high-side device is in the ON state, the potential of the middle point (reference of the sensor) is very close to DC+, which makes the diode D11 forward biased. Device S2 being in the OFF state, sees the full DC bus voltage across its terminals, which makes diode D21 reversed biased. Similarly, when the high-side device is in the OFF state and the low-side device is in the ON sate, diode D11 becomes reversed biased and diode D21 becomes forward biased. Thus, although the sensor is connected to the HB and across the DC bus, the high voltage is blocked either by diode D11 or by diode D21.

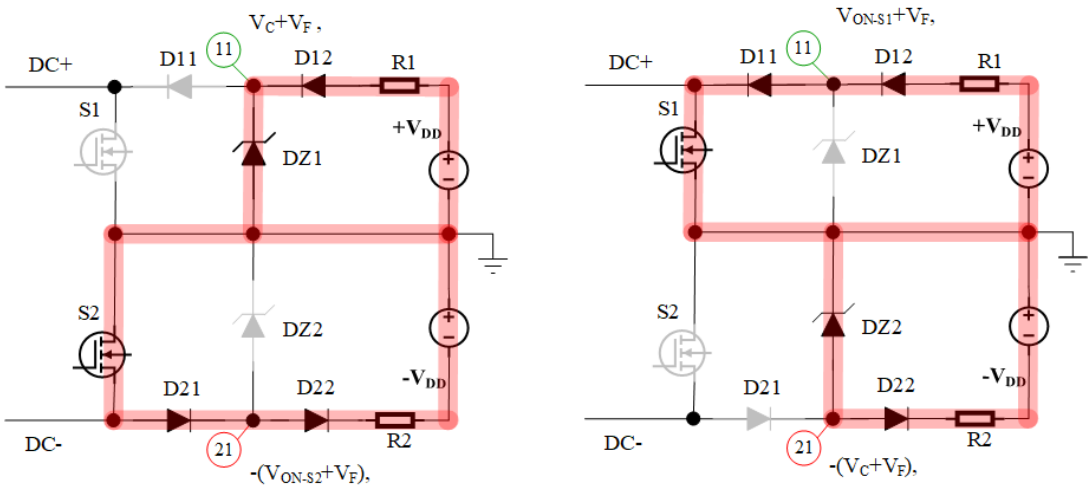

Figure 3.15: Voltage clamping stages of the proposed half-bridge V_{DSON} sensor. High-side device (S1) is turned on (left) and the low-side device (S2) is turned on (right). Highlighted parts showing the active components of the circuit and faded parts indicated a non-conducting state

Figure 3.15 (right) illustrates the HB and HBV_{ON} sensor interaction when the high-side device is in the on-state and the low-side device is in the off-state. At this condition, the node voltage at node 11 measures $V_{ON-S1} + V_F$, where V_{ON-S1} is the on-state voltage of the high-side device (S1) and V_F is the forward voltage drop of the diode D11.As the low-side device (S2) is off during this period, the node voltage at node 21 measures a constant voltage $-(V_C + V_F)$.

Figure 3.15 (left) illustrates the HB and HBV_{ON} sensor interaction when the low-side device is in the on-state and the high-side device is in the off-state. At this condition, the node voltage at node 21 measures $-(V_{ON-S2} - V_F)$, where V_{ON-S2} is the on-state voltage of the low-side device (S2) and V_F is the forward voltage drop of the diode D21. As the high-side device (S1) is off during this period, the node voltage at node 11 measures a constant voltage $V_C + V_F$. The constant voltage V_C is known and defined by the Zener diodes (DZ1, DZ2), series connected diodes (D12, D22), series resistors (R1, R2) and the power supplies (+VDD, -VDD).

The second stage measures the diode (D12 and D22) forward voltage drop with differential amplifier circuits. The voltage drop across these diodes are expected to be same as the voltage drop across diodes D11 and D21 respectively when same current flows through them, which is the case during the on-state.

The third state subtracts the measured forward voltage drop from the first stage measurement to get V_{ON}.

The fourth stage of the sensor combines the signals from the low-side and high-side circuits (node 13 and 23). The combined signal contains V_{ON} of either the high-side or the low-side device whichever is in the on-state and the constant voltage VC.

Table 3.2: Analog circuit operation of the half-bridge V_{DSON} sensor at different nodes.

Analog circuit operation	Output node	S1: ON, S2: OFF	S1: OFF, S2:ON
Voltage clamp circuit	11	V_{ON-S1}+V_F	V_C+V_F
Voltage clamp circuit	21	-(V_C+V_F)	-(V_{ON-S2}+V_F)
Diode forward voltage measurement	12	V_F	V_F
Diode forward voltage measurement	22	V_F	V_F
V_{11}-V_{11}	13	V_{ON-S1}	V_C
V_{21}-V_{21}	23	-V_C	-V_{ON-S2}
V_{13}-V_{23}	4	V_{ON-S1}+V_C	V_{ON-S2}+V_C
V_4-V_C	5	V_{ON-S1}	V_{ON-S2}
Isolation	6	V_{ON-S1}	V_{ON-S2}

In the fifth stage, an offset voltage generator generates a voltage equal to V_C, the voltage offset present at the output of the fourth stage. This voltage offset is then subtracted from V4 to get the final V_{ON}, V5. The final V_{ON} contains V_{ON} of the

device which is in the on-state. The sixth stage is the isolation stage, which translates the final output to the control circuit reference so that the final V_{ON} sensing output can be connected to a DSP or an ADC input pin for further in-situ health monitoring.

The operation and the output of each of the signal stages are presented in Table 3.2. The node voltages are named in reference to the nodes illustrated in figure 3.14. The fundamental operating principle and the ideal waveform at some major nodes and the final output of the sensor are presented in figure 3.16.

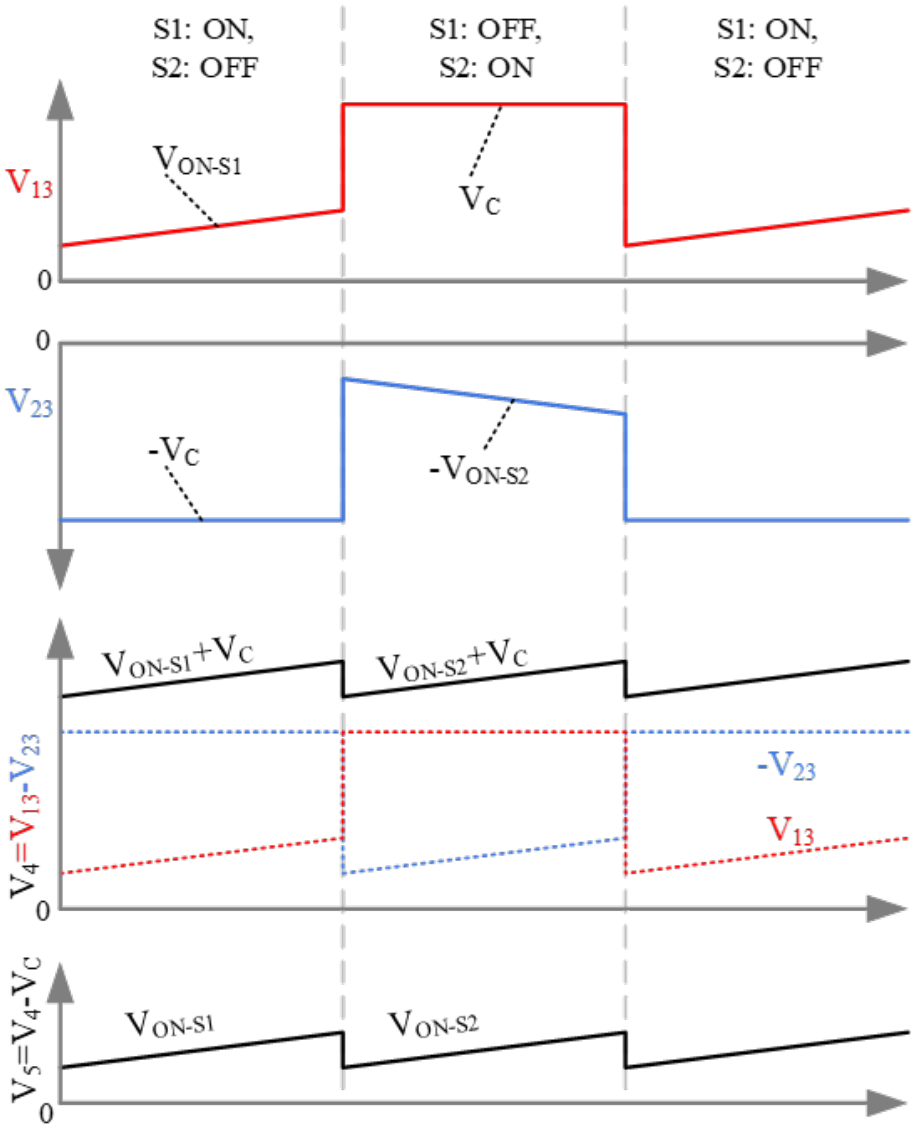

Figure 3.16: Ideal waveforms at different nodes of the HBV_{DSON} sensor.

3.2.2 Sensor board and experiment results

The HBV_{DSON} sensor has been designed and integrated with the gate driver board for a 1200V SiC HB module. The PCB board hardware prototype is presented in 3.17. Individual validation of the circuit stages of the V_{ON} sensor was completed prior to V_{ON} performance evaluation under switching.

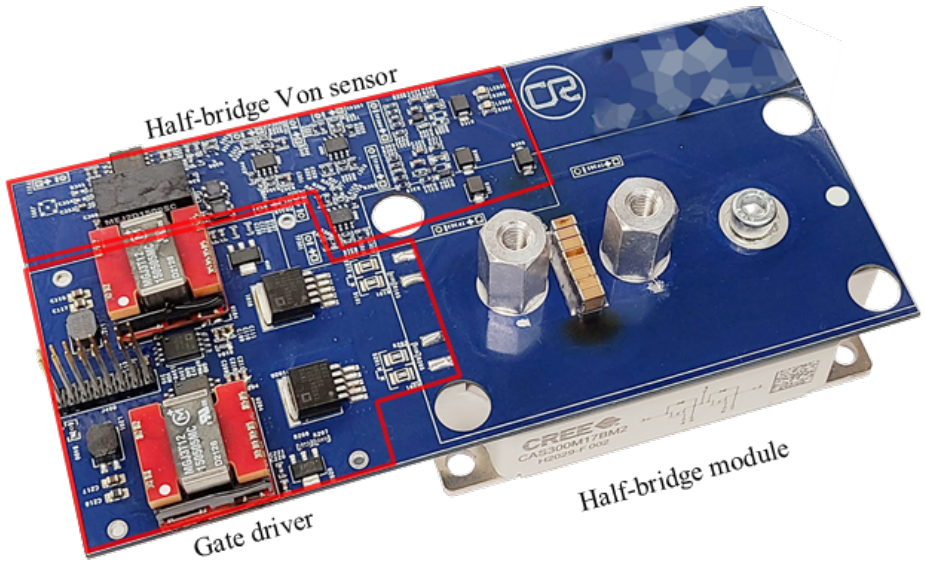

Figure 3.17: Designed PCB of the half-bridge V_{DSON} sensor integrated with the gate driver board. The sensing board provides V_{DSON} of both high and low-side MOSFETs in one output signal.

3.2.3 Sensor performance validation under DC conditions

First, the on-state voltage accuracy of the sensor is quantified under DC conditions. To calculate the accuracy of sensor reading at the entire range of input, the configuration presented in Fig. 6 is used. Where both of the devices are kept in the off-state and a variable resistor is connected across one of the two devices. The variable resistor is used to create a small voltage across the input terminals of the V_{ON} sensor under test and is varied to get a voltage from 0V to 2V at the input terminals. When the variable resistor is connected to the high side of the sensor, it represents a situation when the low-side device is in the off-state and the high-side

device is in the on-state. Similarly, when the variable resistor is connected to the low side of the sensor, it represents a situation when the high-side device is in the off-state and the low-side device is in the on-state. Although in both cases, both the high-side and low-side devices are in the off-state, this configuration is necessary to provide the small, temperature-independent DC voltage across one SiC FET of the half-bridge module, and a large DC voltage across the other side as series operation of benchtop supplies is discouraged at hundreds of volts. At every input voltage, the voltages at different sensor nodes are recorded and presented in Table 3.3 and Table 3.4.

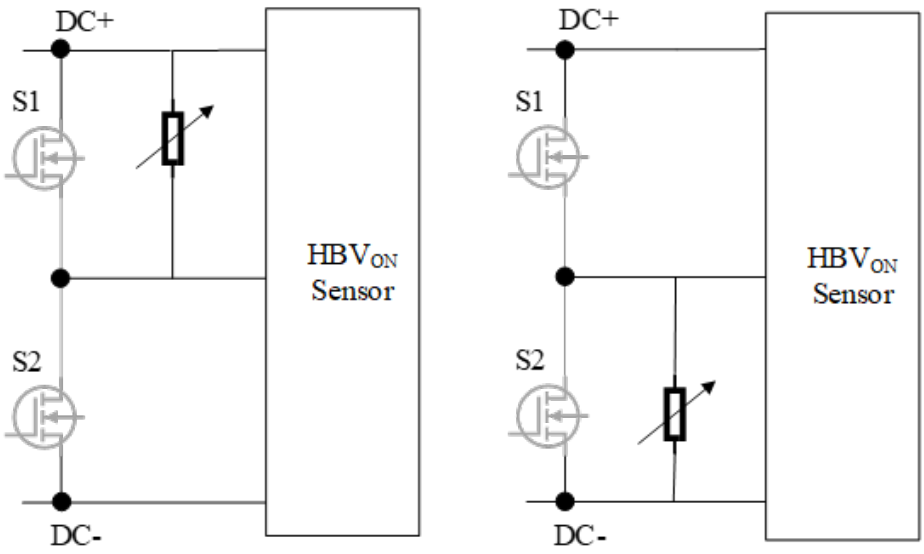

Figure 3.18: Sensor characteristics for different V_{DSON} of the high-side and low-side MOSFETs up to 2V. (left) Input applied to the high-side, low-side device turned off. (right) Input applied to the low-side, high-side device turned off.

Table 3.3 presents the measurements and accuracy of the high-side V_{ON} sensor and 3.4 presents the measurements and accuracy of the low-side V_{ON} sensor. From the DC measurements, it can be seen that the non-isolated final output has a very small error <4% for input voltages of 0.58 V or higher. At lower input voltages the error is relatively large which is due to the low signal-to-noise ratio. The isolated output of the sensor also has a very small error <4% for inputs from 0.58V or higher.

These errors, however, could be adjusted with appropriate calibration with the data presented in the tables.

Table 3.3: DC characteristics of HBV_{DSON} the sensor, high-side device as DUT, and the low-side device turned off.

Input(V)	Final output (V5) (V)	Error (V)	Error (%)	Isolated output (V)	Error in isolated output (V)	Error in isolated output (%)
0.106	0.128	0.022	20.75%	0.092	0.014	13%
0.308	0.332	0.024	7.79%	0.292	0.016	5%
0.577	0.600	0.023	3.99%	0.557	0.020	3%
1.359	1.377	0.018	1.32%	1.326	0.033	2%
1.645	1.657	0.012	0.73%	1.603	0.042	3%
2.014	2.017	0.003	0.15%	1.958	0.056	3%

Table 3.4: DC characteristics of the HBV_{DSON} sensor, low-side device as DUT, and the high-side device turned off.

Input(V)	Final output (V5) (V)	Error (V)	Error (%)	Isolated output (V)	Error in isolated output (V)	Error in isolated output (%)
0.106	0.128	0.022	20.75%	0.086	0.020	19%
0.310	0.332	0.022	7.10%	0.292	0.018	6%
0.582	0.602	0.020	3.44%	0.559	0.023	4%
1.370	1.382	0.012	0.88%	1.332	0.038	3%
1.652	1.660	0.008	0.48%	1.605	0.047	3%
2.016	2.016	0.002	0.10%	1.955	0.061	3%

3.2.4 Sensor performance validation in double pulse test

In addition, to quantifying the accuracy under DC conditions, the sensor performance is evaluated under switching conditions as well. To evaluate dynamic performance, a double pulse test (DPT) is conducted. In the DPT, one device is used as the device under test (DUT) while keeping the other in the off-state. All the major sensing nodes are recorded with a 200V input DC bus. Oscilloscope captures at different nodes are presented in figure 3.19 and figure 3.20. When the high-side device is used as the DUT, the high-side sensing part of the HBV_{ON} sensor measures the V_{ON} of the high-side device during its on-state while the low-side sensing part measures a constant voltage. After addition and offset compensation, the final isolated output of the HBV_{ON} sensor provides the V_{ON} of the high-side device. During the off-state of the DUT, the high-side sensing part of the sensor measures a constant voltage, but the low-side sensing part of the device measures negative voltage as current flows through the body diode of the low-side device during this period. This negative voltage is clamped at the final sensor output. Thus, the final sensor output provides the V_{ON} of the high-side device when it's ON and a zero voltage when it's OFF.

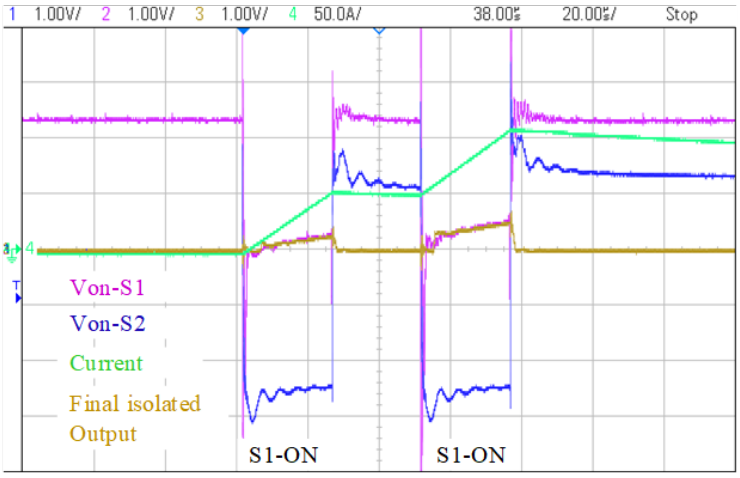

Figure 3.19: DPT waveforms. Only the high-side device is used as the DUT while keeping the low-side device turned off. The test is conducted at 200V DC bus voltage.

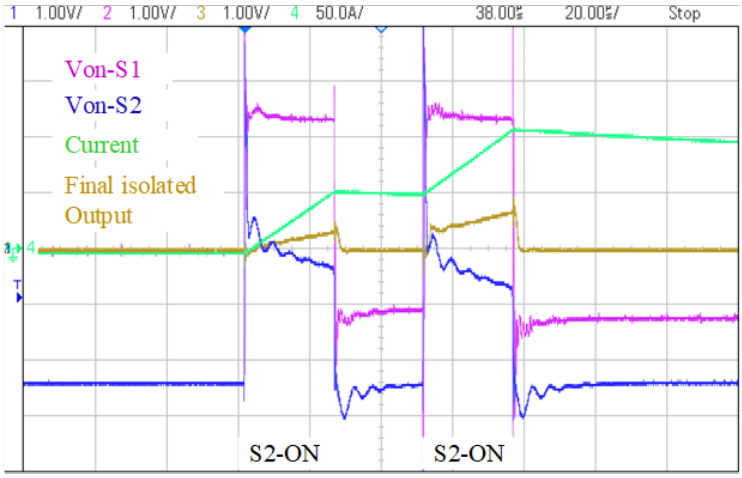

Figure 3.20: DPT waveforms. Only the low-side device is used as the DUT while keeping the high-side device turned off. The test is conducted at 200V DC bus voltage.

Similarly, when the low-side device is used as the DUT, the sensor final output provides V_{ON} of the low-side device when it's ON and a zero voltage when it's OFF.

Using the measured V_{ON} and the current information from the captured data, the on-state resistance of the DUTs is calculated and presented in figure 3.21 and figure3.22. A CREE 1200V module CAS300M12BM2 [69] is used for the DPT. The reported on-state resistance of this module in the datasheet is from 4.17 mÎ© (typical) to 5.67 mÎ© (max). Calculated on-state resistance using the output of the HBV_{ON} sensor and current reading from a TektR_{ON}ix current probe is found to be in the same range. The exact accuracy of the calculated resistance is not reported from the test as the true R_{ON} of the module was not measured using any other tools for reference. Even if the exact accuracy is not reported, the measured R_{ON} is well within the datasheet provided range.

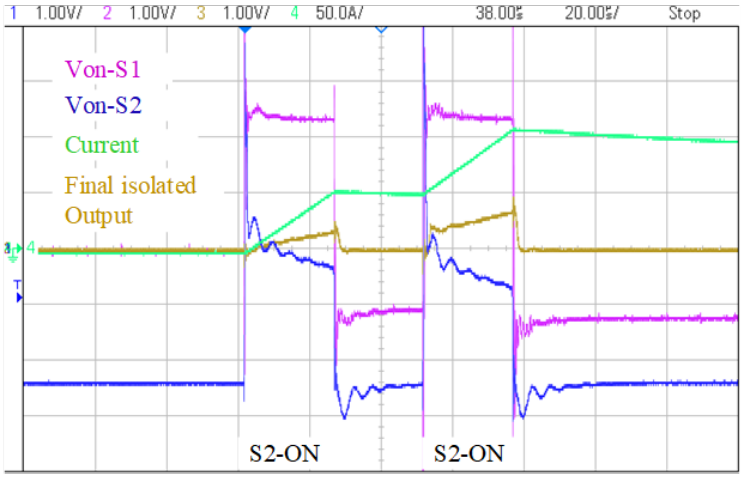

Figure 3.21: R_{DSON} calculation using HBV_{DSON} sensor DPT waveforms: high-side MOSFET as DUT.

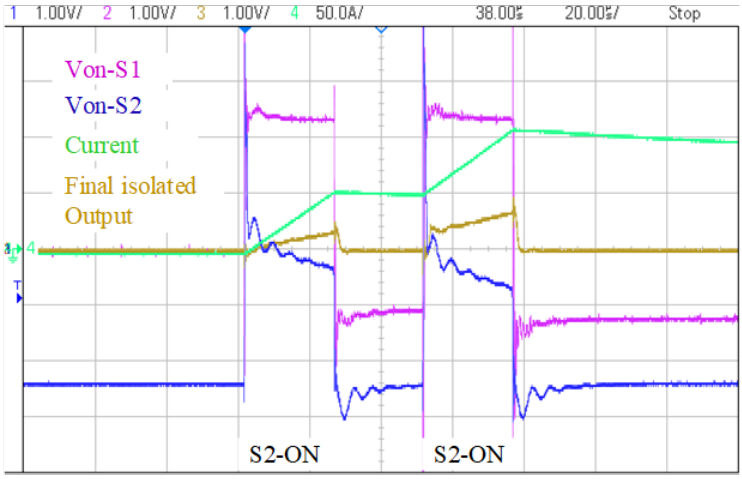

Figure 3.22: R_{DSON} calculation using HBV_{DSON} sensor DPT waveforms: low-side MOSFET as DUT.

3.2.5 Validation of the HBV_{DSON} sensor in complementary switching

The final experiment is conducted with the HBV_{DSON} sensor when the HB is used in a practical operation where the high-side and low-side devices are turned on and off in a complimentary manner. In this test, for a half-cycle, the high-side device is turned ON and, for the remaining half-cycle, the low-side device is turned ON. The test setup is built as a full-bridge (FB) configuration with a series inductor and resistor load connected between the two HBs. This FB circuit is built to represent a

real-world application of two HB modules as a single-phase inverter. The HBV_{DSON} sensor is connected to two DUTs (S1 and S2) of one of the two modules. The FB is controlled in a complementary switching manner i.e. S1 and S4 were turned on/off together while S2 and S3 together were in the complementary state.

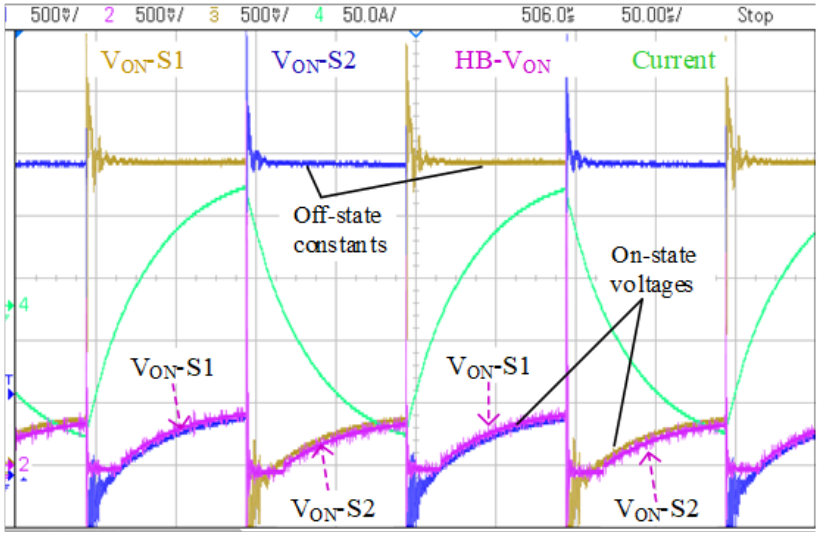

Figure 3.23: Experiment results in a full-bridge configuration. HBV_{DSON} sensor measurements in complementary switching.

Figure 3.23 presents the sensor waveforms of the high-side V_{DSON} and low-side V_{DSON} as well as the combined sensor output that contains V_{DSON} of two DUTs depending on their ON/OFF status. The intermediate sensor node that measures the individual V_{DSON} of the high-side and low-side devices shows the V_{DSON} during their on-state and a constant voltage during their off-state. The final output does not have the offset and contains HBV_{DSON} of both devices as only one device was in the on-state at a time. The final sensor output is used to calculate the R_{DSON} of both DUTs. Figure 3.24 presents the calculated R_{DSON} of both devices. The same inductor current is used to calculate the R_{DSON} of both DUTs. The inductor current is in the same direction as the current through the high-side device (S1) but in the opposite direction to the current through the low-side device (S2). Therefore, the calculated R_{DSON} of the low-side device is represented as negative which is due to

the negative sign of the current. The calculated R_{DSON} of both devices is very close to the DPT results and within the range of values provided in the datasheet.

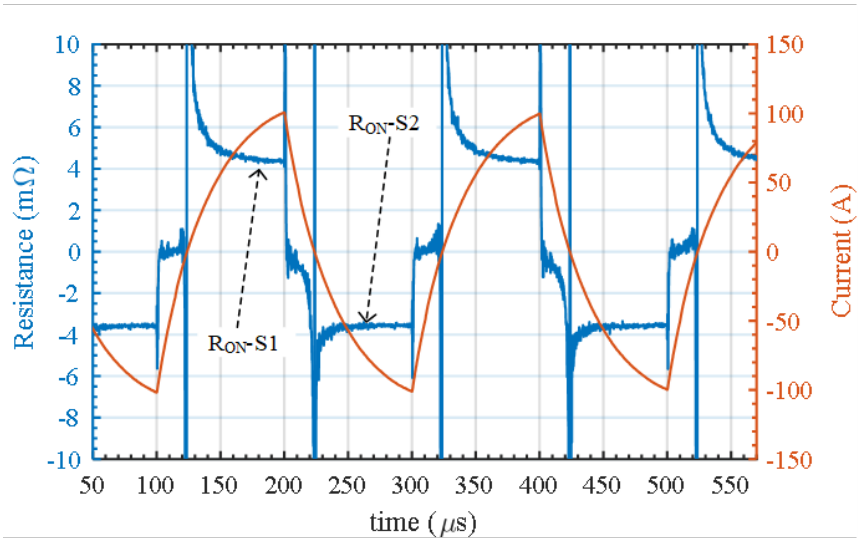

Figure 3.24: Experiment results in a full-bridge configuration. R_{DSON} calculation in complementary switching.

One major drawback to this compensation scheme is the indirect estimation of the blocking diode forward voltage drop. As the forward voltage of the blocking diode can not be measured directly during operation, it is estimated using the series diode having similar characteristics. And during the DUT on state, the same current flows through the two series-connected diodes (D1-D2 and D3-D4). Even if two diodes are picked from the same production batch, they still have a small mismatch in their forward characteristics which introduces some errors in the measurements. Therefore, this mismatch in diode characteristics needs to be taken into consideration during sensor design. For this application, the characteristics are matched manually by checking the forward voltage drop at a certain current and using the pair having a similar voltage drop in one circuit to reduce error.

CHAPTER 4: ONLINE IN-SITU R_{DSON} MONITORING IMPLEMENTATION IN A 75kW THREE-PHASE INVERTER

4.1 V_{DSON} sensor integration for online in-situ R_{DSON} monitoring

Two measurements are required for in-situ R_{DSON} measurement of a MOSFET, the V_{DSON}, and I_{DS}. The measured signals need to be translated into the control reference to convert into digital data for further processing. The conventional voltage clamping circuit measures the V_{DSON} referenced to the source of the MOSFETs. This method allows for the same measurement reference of the V_{DSON} sensing circuits for the three low-side MOSFETs but does not provide a single measurement reference of the high-side MOSFETs. Therefore, the conventional circuit has been modified to simplify the circuit, and a new circuit is proposed to have a single measurement reference of V_{DSON} sensing circuits for the high-side MOSFETs. The R_{DSON} sensing architecture for the three-phase inverter using this new circuit for the high side is presented in figure 4.1.

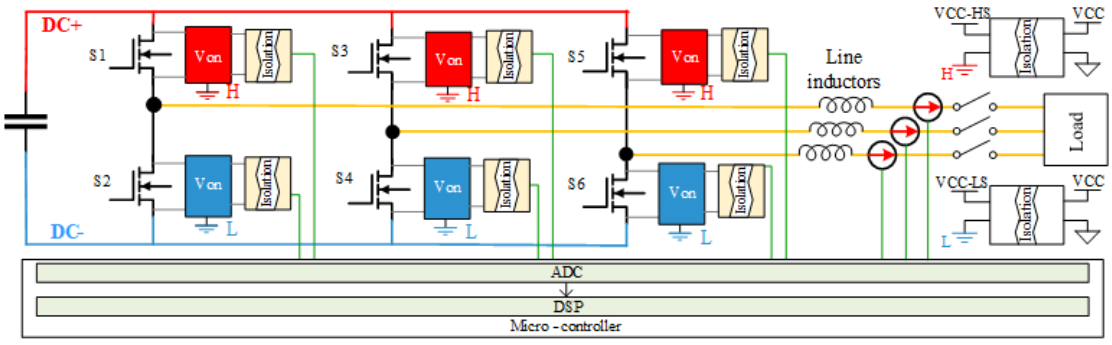

Figure 4.1: Sensing circuit integration architecture of the online in-situ R_{DSON} monitoring.

For the R_{DSON} calculation, I_{DS} is required along with the V_{DSON}. However, adding a current sensor in the switching loop on the drain or source side adds parasitic

inductance, increasing loss and creating higher voltage overshoots and undershoots. Instead of adding the current sensor to the drain or source of the MOSFETs, it is connected to the outputs of the half-bridges, as presented in figure 4.1. The line current is good enough for the steady-state R_{DSON} calculation as the steady-state line current is the same as the MOSFET current during the on-state. A commercial off-the-shelf current sensor is used for the current measurement. Therefore, details of the current sensor are not discussed in this paper. Furthermore, the proposed architecture is minimally invasive to the existing inverter architecture. It requires electrical connections to only three outputs of the three half-bridges and the DC bus. This minimally invasive architecture can be implemented on an existing inverter setup with minimal modifications to the hardware.

4.2 Online in-situ R_{DSON} calculation and reporting

The V_{DSON} and I_{DS} sensor outputs are sampled and processed through a digital microcontroller (DSP) for the real-time R_{DSON} update feature. The sampled data go through a series of data qualification stages to achieve an accurate and meaningful measurement.

4.2.1 Data sampling and synchronization for online R_{DSON} calculation

The first step is reading the V_{DSON} and I_{DS} sensor outputs using the analog-to-digital converter (ADC) module in DSP. Synchronization of ADC sampling with the pulse width modulation (PWM) signal is one of the important implementation considerations. As shown in figure 4.2, the effective V_{DSON} and I_{DS} waveforms (blue lines) appear when the device is on. Hence, the ADC sampling needs to be completed within this short time period. In particular, the center of the PWM on time (tPWM,Center) is the preferred area for accurate ADC sampling by avoiding the potential signal noise near the PWM switching transitions. In fact, three AC inductor currents (ILa, ILb, ILc) used for the primary inverter functions such as closed-loop

control and protection are already sampled at tPWM,Center.

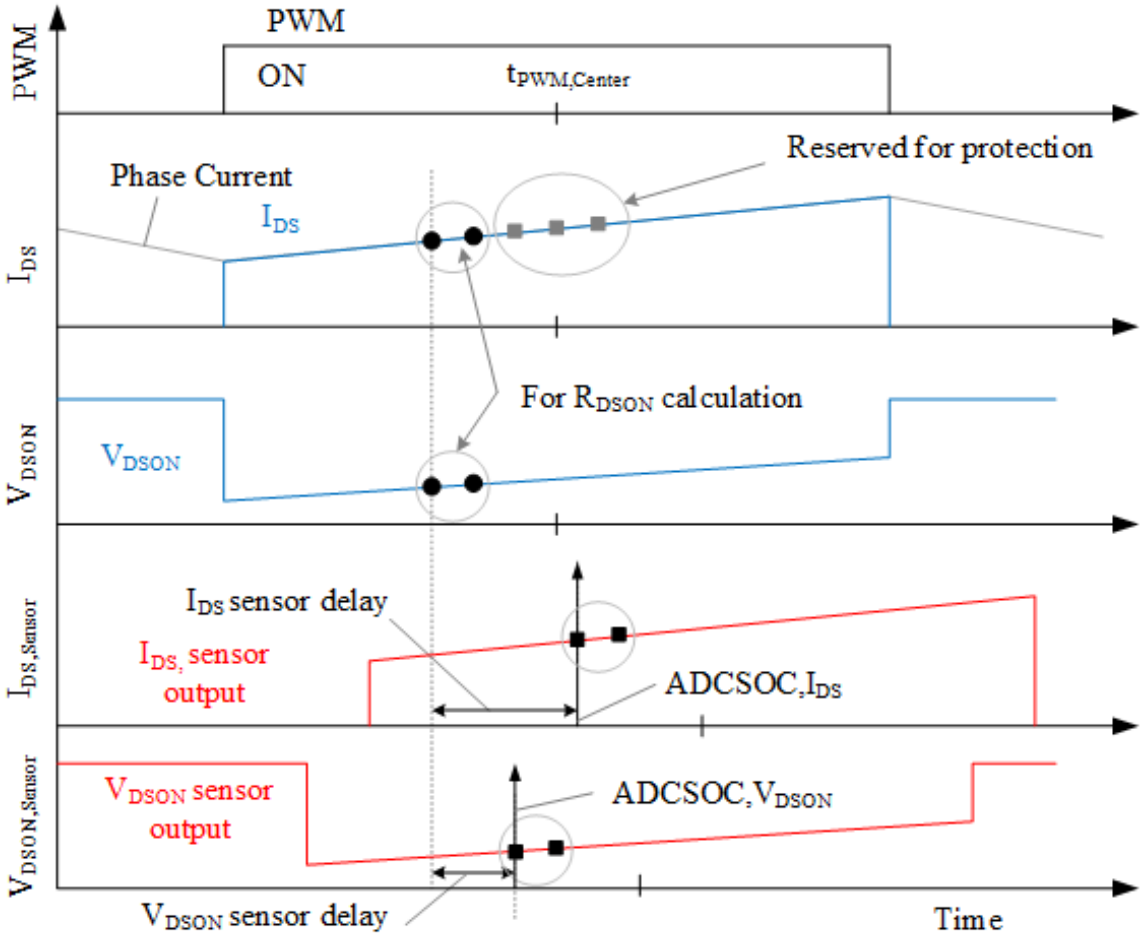

Figure 4.2: V_{DSON} and I_{DS} sampling synchroization for instantaneous R_{DSON} calculation. Blue lines indicate the ideal current and voltage waveforms, and the red lines represent the measured signals. The measurement delay is characterized to align the current and voltage measurements.

Two additional samples of each V_{DSON} and I_{DS} are captured for the online R_{DSON} calculation. These V_{DSON} and I_{DS} measurements are captured before the three AC inductor current samples, as shown in 4.2. ADC Start-Of-Conversion (SOC) triggers, ADCSOC,I_{DS} and ADCSOC,V_{DSON}, are programmed to start sampling V_{DSON} and I_{DS}. The V_{DSON} and I_{DS} sensing circuits have different signal output delays, as shown in 4.2 (red lines). These delays are characterized through experiments and presented in the next section. To compensate for these sensing delays, the two ADCSOC triggers

are shifted independently to synchronize the V_{DSON} and I_{DS} measurements.

4.2.2 Data qualification to filter noisy data from calculation

Due to practical issues of hardware circuit components, false or noisy sensing output signals may inadvertently be applied to the microcontroller. The first challenge is that the isolated analog amplifier, ADuM4190, has a lower common-mode input range, which does not provide accurate isolated output for inputs that is less than 200 mV. To address this limitation, R_{DSON} is only calculated above 30 A phase current of the inverter. 30 A phase current corresponds to 210 mV voltage drop across the drain and source terminal of the MOSFET considering $7m\Omega$ R_{DSON}. In addition, switching transitions of other phases cause EMI noise on the V_{DSON} and I_{DS} sensing signals, even though the ADC readings are synchronized near the tPWM,Center. It is confirmed that a switching event when the modulation index (of the phase being sampled) is less than 0.85 provides enough time to avoid the switching noise interference from other phases and have noise-free ADC samples. Therefore, the effective range of the modulation index for the R_{DSON} measurement is limited to less than 0.85. The data qualification flow chart is shown in figure 4.3.

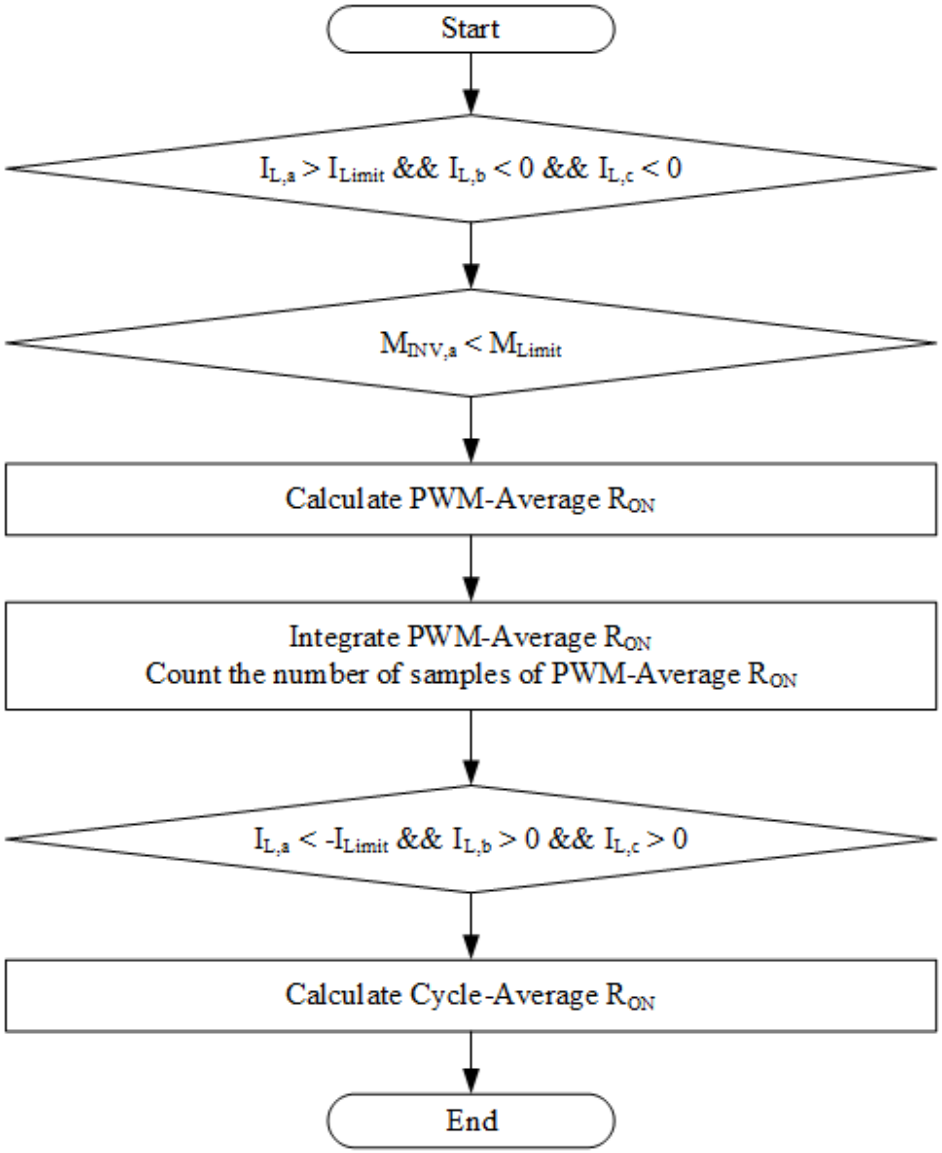

Figure 4.3: Developed flow chart for R_{DSON} calculation: Example is shown only for one device, the phase A high-side MOSFET. This is repeated sequentially to get R_{DSON} of all six MOSFETs in one AC-cycle.

4.2.3 Average R_{DSON} calculation and reporting

When calculating R_{DSON}, multiple samples of R_{DSON} values are averaged to minimize random fluctuations of the measured data. The PWM-average R_{DSON} is calculated by averaging two samples of R_{DSON} data obtained within a single PWM cycle. The PWM-average R_{DSON} values are integrated during the acquisition window shown in figure 4.4, and the R_{DSON} sum is divided by the number of PWM cycles counted

during the acquisition window. The resulting value of this averaging process is called cycle-average R_{DSON}. The cycle-average R_{DSON} is obtained at the beginning of the acquisition window of the opposite device in the same phase leg. This calculation timing is designed to cope with the variation in the width of the acquisition window, which varies according to the inverter's operating condition. All six cycle average R_{DSON} data are updated every fundamental frequency cycle.

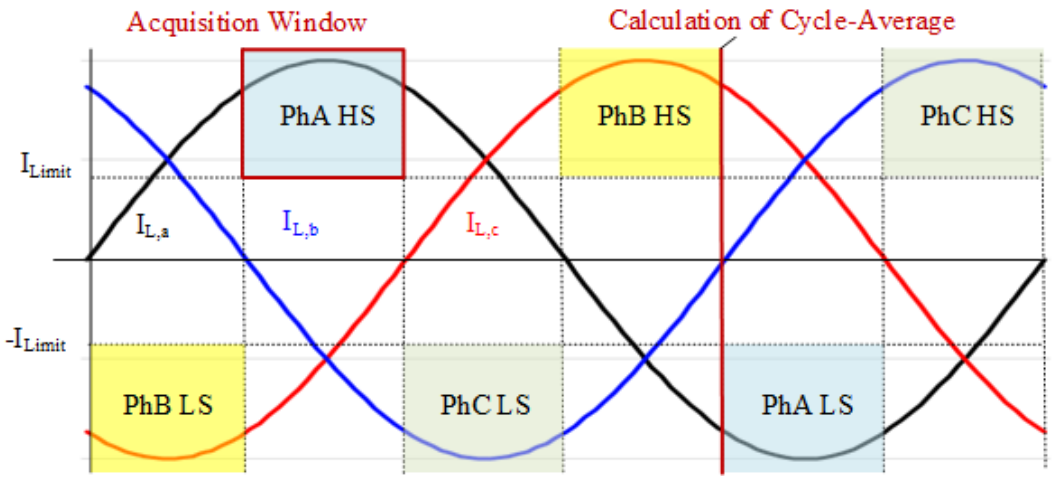

Figure 4.4: Three-phase Current and Voltage sampling window. Shaded areas indicate the current and voltage data acquisition window for the six MOSFETs. The average is calculated at the beginning of the data acquisition of the complementary device of the same leg.

4.3 Hardware setup and experiment results

The in-situ R_{DSON} monitoring is implemented on a 75 kW three-phase inverter. The specification of the inverter is presented in Table 4.1. The inverter consists of different boards assembled together, an exploded view of the 3D image of the inverter assembly is presented in figure 4.5. The primary components of the assembly are the baseplate that houses all the components, the SiC MOSFET modules, V_{DSON} sensing board, DC-bus and decoupling capacitor boards, gate driver boards, output current sensors, and a motherboard.

Table 4.1: Specification of the three-phase inverter.

Parameter	Value
Maximum rated power	75 kW
Nominal input voltage	1000 V DC
Output voltage	480 V AC
Switching frequency	30 k Hz
SiC module	CAS300M17BM2 [67]

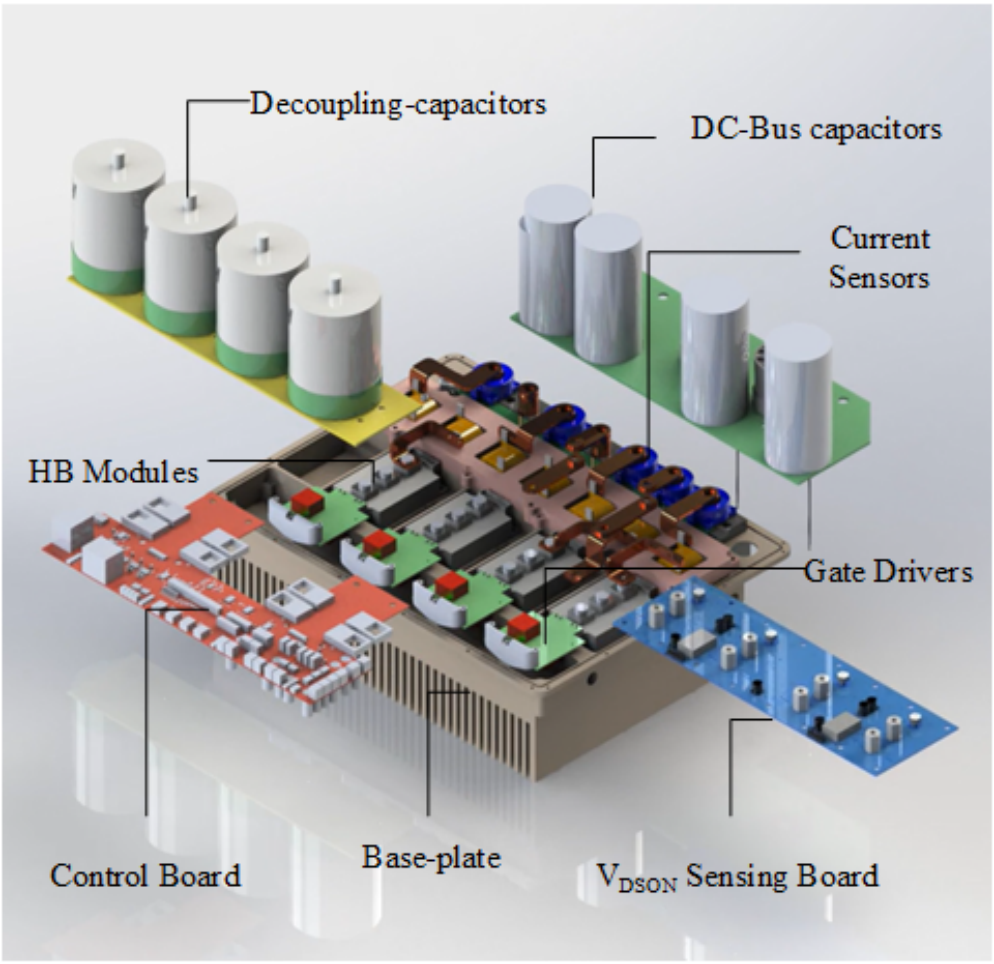

Figure 4.5: Exploded 3D image of the inverter assembly.

Figure 4.6 presents a cross-section of the interconnection among different components of the inverter assembly. The V_{DSON} sensing board is mounted directly on top

of the SiC HB modules. The line current sensors are mounted around the bushing terminals of the output terminals of the inverter. The motherboard has a TI DSP F28379D control card for inverter control and R_{DSON} calculation.

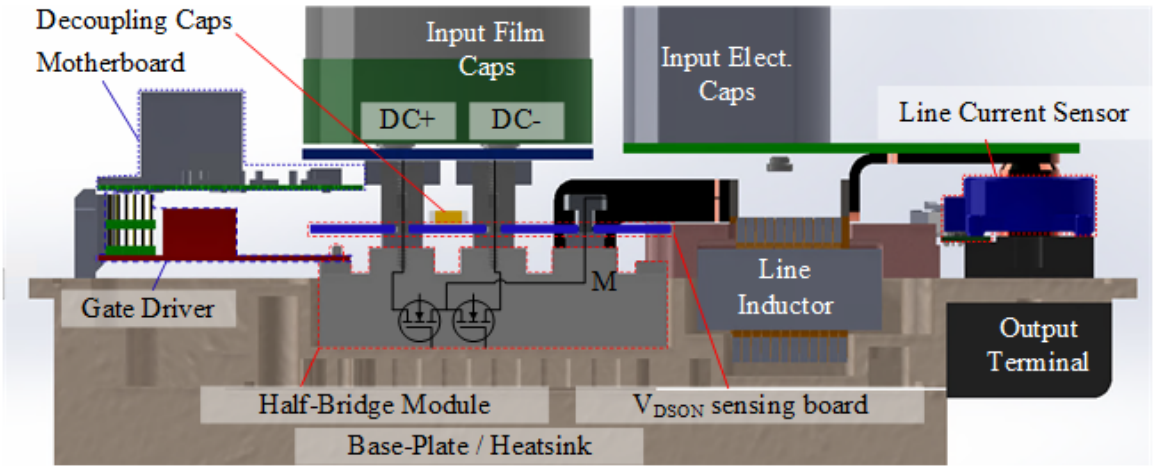

Figure 4.6: Cross-section of the inverter assembly.

Figure 4.7 presents an image of the V_{DSON} sensor board assembly taken from the top. The V_{DSON} board is directly mounted on top of the SiC MOSFET modules to have minimum parasitic impedance between the MOSFET terminals and the sensing terminals. This close assembly also provides for ceramic decoupling capacitor placement that helps the transient switching performance of the inverter.

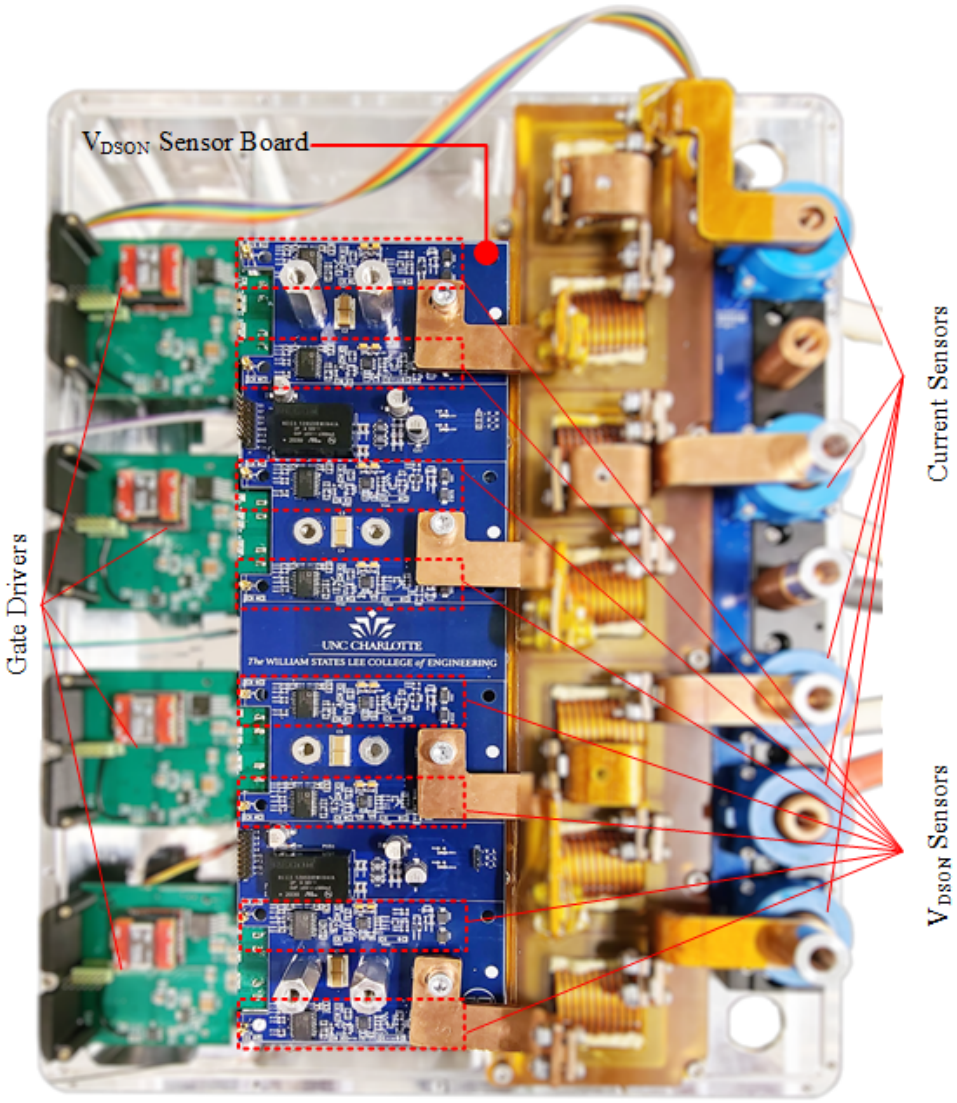

Figure 4.7: V_{DSON} sensor board placement in the inveter.

Several experiments are conducted to validate the online in-situ R_{DSON} monitoring solution. The experiments can be classified into three different operating conditions, (i) DPT, (ii) DC condition, and (iii) sinusoidal inverter operation.

4.3.1 Sensor dynamic characterization in DPT

To find the V_{DSON} and I_{DS} sensor output dynamic characteristics, a DPT is conducted. It has been found that the analog isolator adds 1.2μs time delay in the measured signal of the V_{DSON} sensor. Similarly, the hall effect current sensor adds

$3\mu s$ delay to the measured signal compared to the actual current. The current sensor measurement is compared with a Tektronix current probe (TCP0150), having less than $40ns$ delays. Figure 4.8 presents the delays of the V_{DSON} and I_{DS} sensor outputs. These delays are compensated for later during analog data sampling for the R_{DSON} calculation.

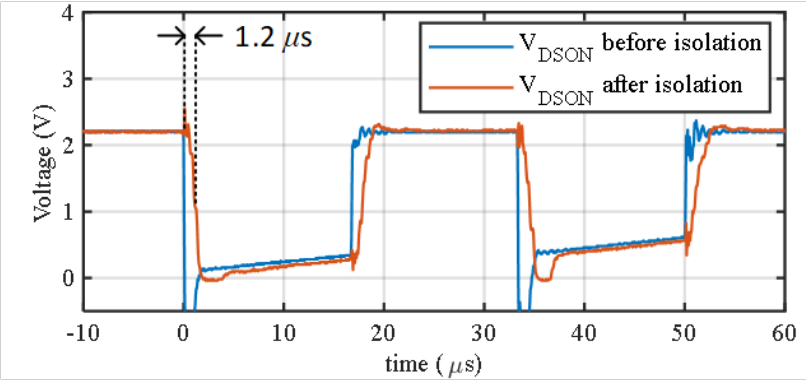

(a) Voltage sensing delay

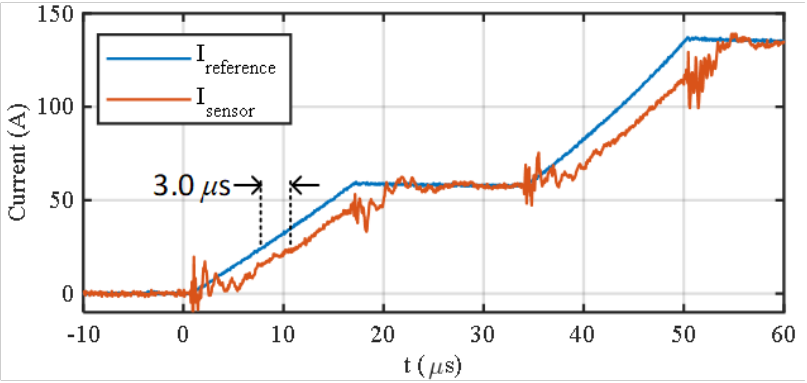

(b) Current sensing delay

Figure 4.8: Experimental evaluation of the voltage and current sensing delays. Isolated V_{DSON} sensor output and current sensor output have 1.2 μs and 3.0 μs delay respectively.

4.3.2 True R_{DSON} reference generation under DC

The actual DC R_{DSON} of the three modules used in the inverter is measured using precision digital multimeters (DMMs). It is a necessary process to obtain the true R_{DSON} data of the specific SiC MOSFET devices we used to validate the online in-situ

R_{DSON} measurement results.

The circuit diagram of the experiment setup and the measured R_{DSON} are presented in figure 4.9. A current source is connected to the DUT with a series-connected precision shunt resistor. The voltage across the DUT and the shunt are measured using DMMs. Then the R_{DSON} is calculated using the DMM measurements. Figure 4.10 presents the measured DC true R_{DSON} of the six MOSFETs from 30A to 100 A device current.

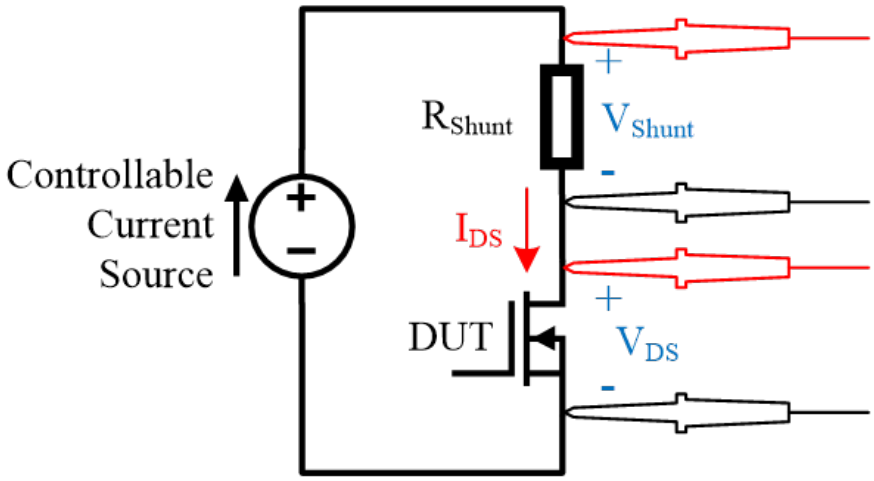

Figure 4.9: Schematics of the DC R_{DSON} characterization for reference generation.

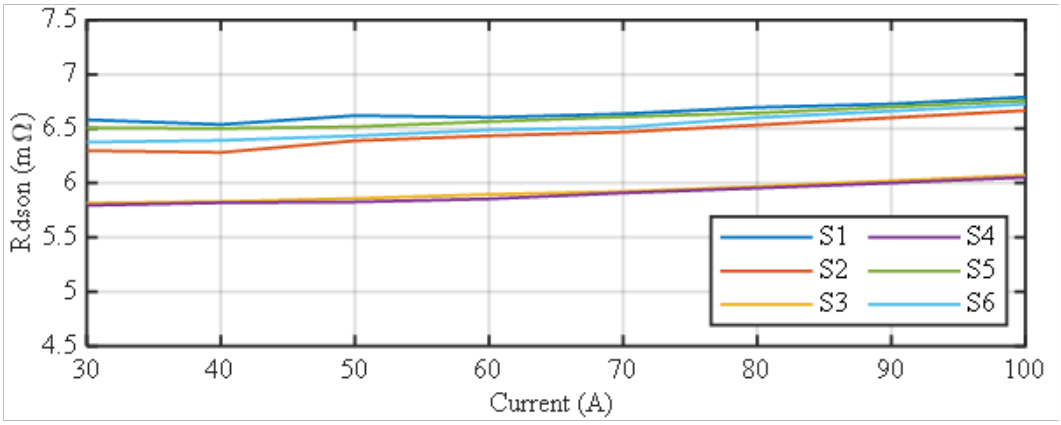

Figure 4.10: True R_{DSON} of the three SiC modules used in the inverter. R_{DSON} is calculated using the current and voltage reading from digital multi-meters..

Figure 4.11 presents the error between the R_{DSON} calculated using the DMMs and

data recorded on the integrated DSP in the inverter motherboard. This figure shows the accuracy of the DSP measurement having an error of less than $0.2m\Omega$ under the entire current level.

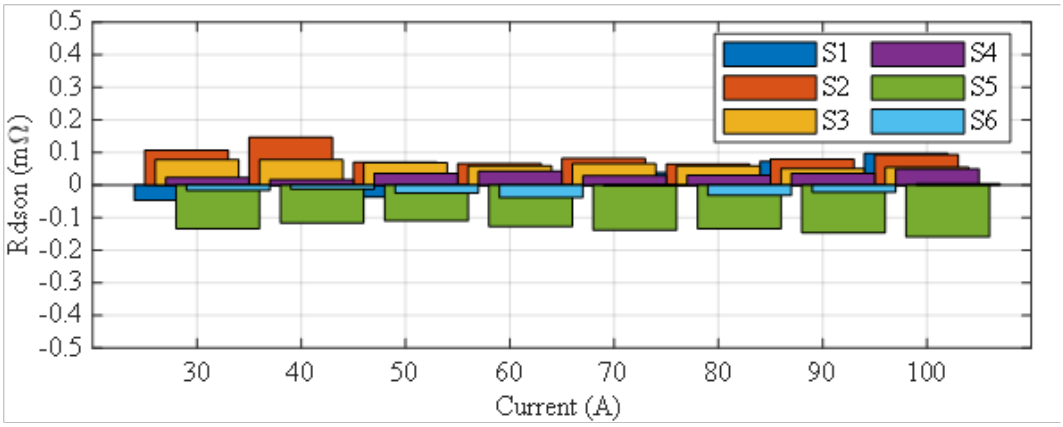

Figure 4.11: Error in the measurement recorded in the DSP compared to the R_{DSON} calculation using the digital multi-meters.

The R_{DSON} of the six MOSFETs at 40A current is listed in Table 4.2. The R_{DSON} of the six MOSFETs are $6.6m\Omega, 6.4m\Omega, 5.9m\Omega, 5.8m\Omega, 6.4m\Omega$, and $6.4m\Omega$ for S1, S2, S3, S4, S5, and S6, respectively at 40 A current, which is the selected currency for the AC operation.

Table 4.2: True (DC) R_{DSON} of the six MOSFETs at 40 A current (Experimental results for reference point generation).

Device No	S1	S2	S3	S4	S5	S6
True (DC) R_{DSON} @40A (mΩ)	6.6	6.4	5.9	5.8	6.4	6.4

4.3.3 Online in-situ R_{DSON} measurement in sinusoidal inverter operation

Figure 4.12 presents the fully assembled inverter hardware under test. For regular inverter operation, all six MOSFETs turn ON and OFF simultaneously following the sinusoidal PWM to generate sinusoidal three-phase output. To validate the online in-situ R_{DSON} measurements the inverter is run above 30kW power converting from 1000V DC to 480V three-phase AC. The V_{DSON} and I_{DS} sensor outputs were cap-

tured on the oscilloscope and also the DSP ADC readings were recorded to make a comparison analysis. Figure 4.13 presents the oscilloscope capture of the V_{DSON} and phase current waveforms in phase-A. The V_{DSON} of the high-side MOSFET is proportional to the positive half cycle of the phase current, and the V_{DSON} of the low-side MOSFET is proportional to the negative half cycle of the phase current.

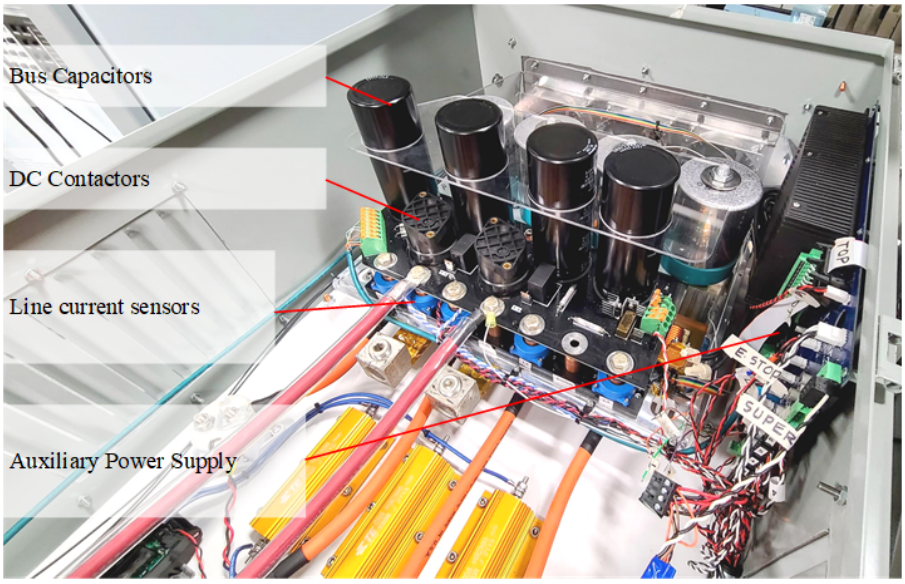

Figure 4.12: The developed hardware prototype.

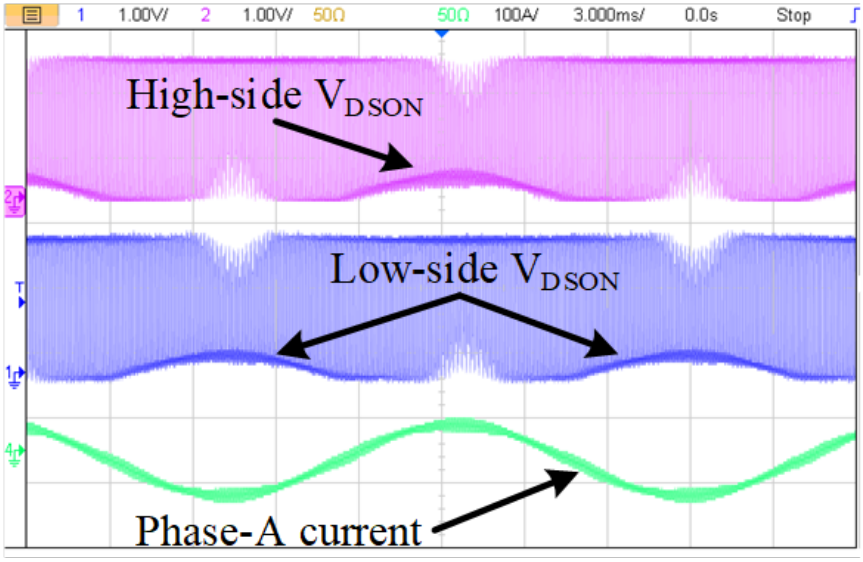

Figure 4.13: Oscilloscope capture under 1000V DC- 480 VAC: Phase A V_{DSON} and phase current measurement.

Figure 4.14 presents the recorded DSP data which is exported for analysis.

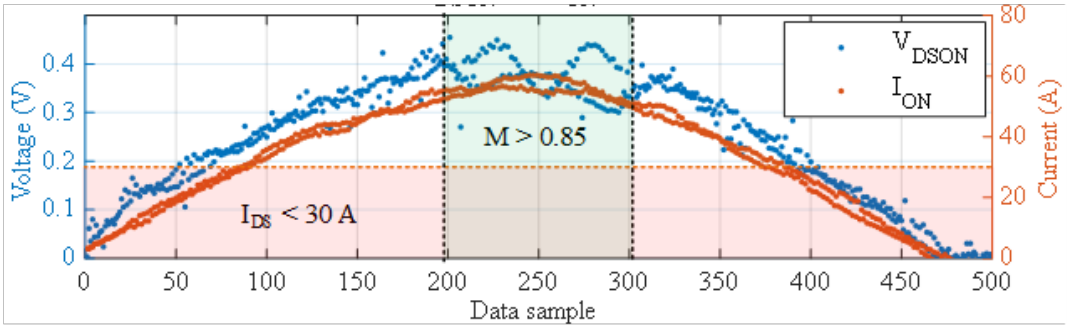

(a) sample V_{DSON} and I_{DS} in the DSP

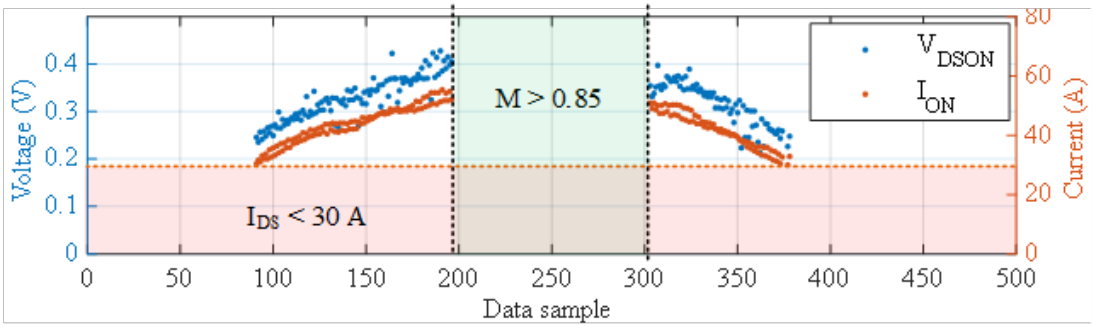

(b) Samples after the data qualifications.

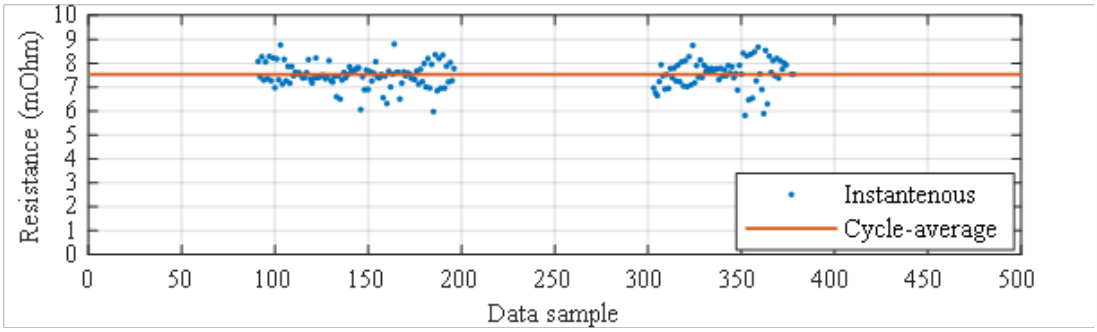

(c) Calculated instantaneous and average R_{DSON}

Figure 4.14: Experimental results under 1000V DC- 480 VAC, data captured on the DSP: Phase A V_{DSON} and current measurement for half grid cycle.

Figure 4.14 (a) presents the sampled V_{DSON} and I_{DS} data points of the Phase-A high-side MOSFET per every switching cycle during the half cycle of the AC output. These data points are recorded on the DSP memory and extracted for validation. At the center of the half cycle, where the modulation index is higher than 0.85, the

switching noise interferences are observed and discarded as per the data qualification algorithm. Figure 4.14 (b) shows data points after the data qualification. After that, PWM-average and cycle-average R_{DSON} values are calculated, as shown in Figure 4.14 (c). These results verify the feasibility and the effectiveness of the proposed in-situ R_{DSON} measurement system architecture and data processing.

For online health monitoring, the cycle averaged R_{DSON} data are recorded and saved. As R_{DSON} is expected to change slowly over a long operating lifetime, the cycle-average R_{DSON} is further averaged every second to reduce the memory requirement to store and process a large number of R_{DSON} data. Figure 4.15 presents recorded averaged R_{DSON} for 300s. The averages of these 300s data points are $7.5m\Omega, 6.8m\Omega, 6.4m\Omega, 6.0m\Omega, 6.9m\Omega$, and $6.9m\Omega$ for S1, S2, S3, S4, S5, and S6, respectively. The R_{DSON} of S3 has some random spikes up to $1m\Omega$ above the average value. A possible reason for the spikes could be the noise source along the propagation path of the V_{DSON}/I_{DS} sensing signal for this MOSFET. Regardless of the spikes, the data is consistent most of the time. Comprehensive analysis of the measured online R_{DSON} is presented in the next section.

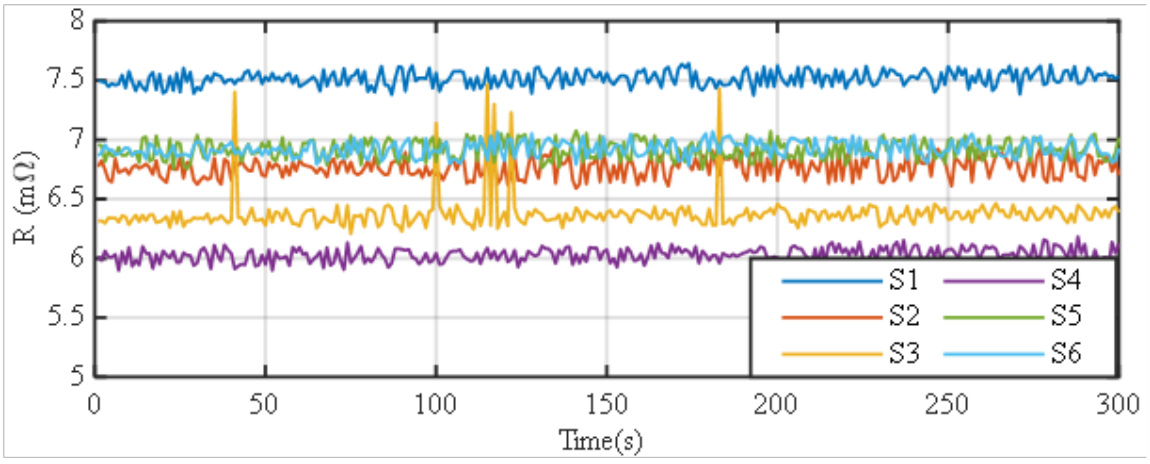

Figure 4.15: Experimental results: In-situ R_{DSON} measurement over 300 s (averaged every 1 s) under 1000V DC-480V AC at 30kW.

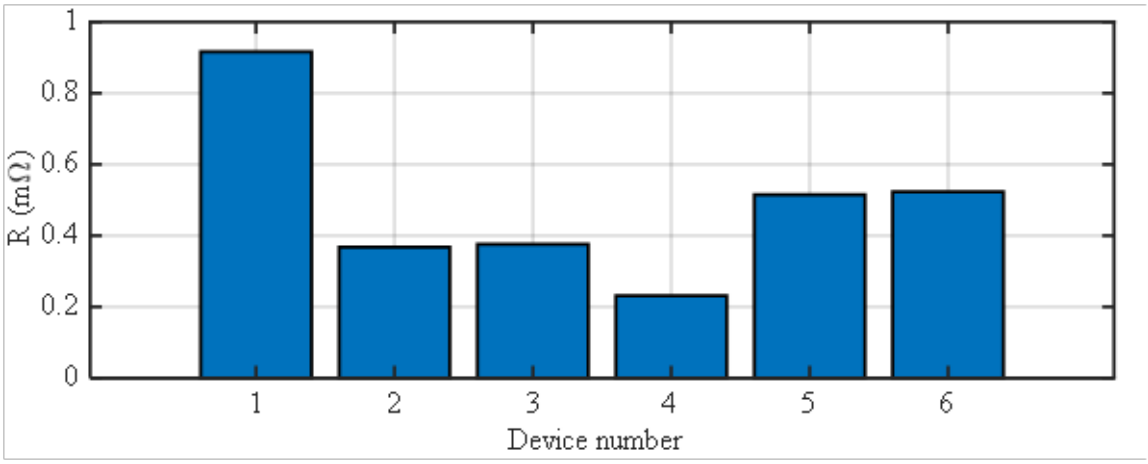

Figure 4.16: Experimental results: Online in-situ AC R_{DSON} increase compared to DC true measurement. The increase in the R_{DSON} is due to the parasitic impedance that adds to the true R_{DSON} under AC conditions

4.3.4 AC impedance analysis

To find the efficacy of the proposed online in-situ R_{DSON} monitoring architecture the true R_{DSON} of each of the six MOSFETs have been characterized under DC conditions to find the baseline R_{DSON}. The details of the DC characterization test are presented in sub-section B. These R_{DSON} references are the true R_{DSON} of the six MOSFETs as these were measured using precision digital multimeters in a controlled condition.

The true (DC) and online in-situ R_{DSON} values at 40A current are picked from figure 4.10 and figure 4.15 and listed in Table 4.3. The online in-situ impedances at 40A current are measured between $6m\Omega$ and $7.5m\Omega$. The average online R_{DSON} of the six MOSFETs at 40A is found to be $6.8m\Omega$, where the average DC R_{DSON} at the same condition from figure 4.10 is $6.3m\Omega$. On average, the online R_{DSON} is $0.5m\Omega$ higher than the DC measurements. This deviation between the DC and online measurement should not be considered as a measurement error but the effect of the parasitic impedances during AC operation. The online measurement includes parasitic elements that increase the impedance as frequency increases. The impedance

seen from the sensor connection point is presented in figure 4.17. Therefore, the measured impedance can be expressed as:

$$\mathrm{Z}_{Meas} = R_{DS}||(1/j\omega C_o) + j\omega L_{stray} + R_{contact} \tag{4.1}$$

Where, Z_{Meas} is the measured impedance, $1/j\omega C_o$ is impedance due to the output capacitance of the DUT, $j\omega L_{stray}$ is the impedance due to the stray inductance and $R_{contact}$ is the contact resistance between the V_{DSON} sensor board and HB module, and ω is the frequency of operation. The typical values of C_O and L_{stray} are given as 2.9 nF and 15 nH for the SiC module (CAS300M17BM2) tested [67]. As an example, if the resistance for DC R_{DSON} is 6.2 $m\Omega$ and the contact resistance is 0.1 $m\Omega$, these values will produce an impedance of

$$\mathrm{Z}_{Meas} = 0.0062||(1/\mathrm{j}\omega \times 2.9 \times 10^{-9}) + j\omega \times 15 \times 10^{-9} + 0.001 \tag{4.2}$$

which results in Z=6.905 $m\Omega$ at 30 kHz, and Z=6.3 $m\Omega$ at DC. Therefore, an increase of 0.605 $m\Omega$ R_{DSON} is expected under AC conditions running at 30 kHz compared to the DC measurements. This increase in the magnitude of impedance, 0.605 $m\Omega$ in this theoretical example based on the datasheet, is in the same range as the measured 0.5 $m\Omega$ average increase of the online in-situ R_{DSON} under sinusoidal AC condition compared to the true (DC) R_{DSON}.

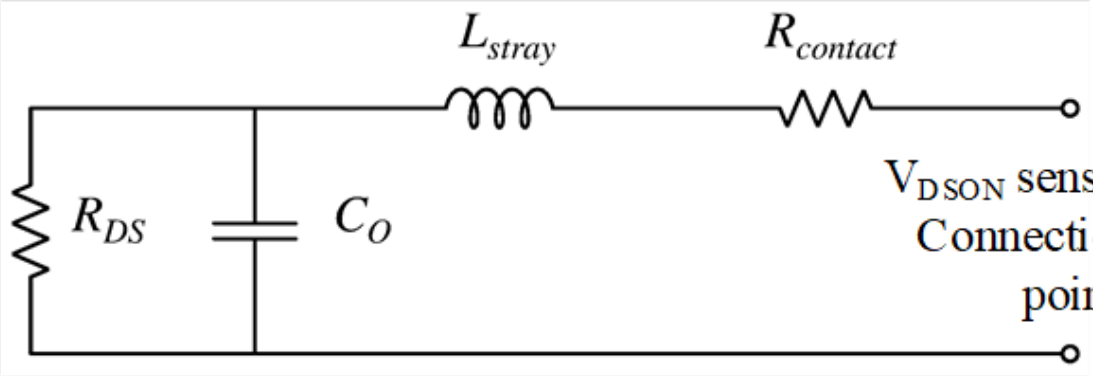

Figure 4.17: Representation of the electrical parasitic elements between the MOSFET and V_{DSON} sensor interconnection.

The difference between the DC R_{DSON} and the in-situ R_{DSON} for the six MOSFETs is presented in Table 4.3.

Table 4.3: Online AC R_{DSON} of the six MOSFETs and true (DC) R_{DSON} under the same operating conditions.

Device No	S1	S2	S3	S4	S5	S6
True (DC) R_{DSON} @40A (mΩ)	6.6	6.4	5.9	5.8	6.4	6.4
AC Online In-situ R_{DSON} @40A (mΩ)	7.5	6.8	6.4	6.0	6.9	6.9
Difference between DC and online R_{DSON} @40A (mΩ)	0.9	0.4	0.5	0.2	0.5	0.5

4.4 Junction temperature estimation using R_{DSON}

Junction temperature is another vital information about the device's instantaneous operational stress. Historical data of MOSFET's junction temperature at a specific operating condition also gives vital information about device aging and degradation. To have another dimension on the device health status, a test setup is developed to find the relationship among the MOSFET junction temperature, V_{DSON}, and I_{DS}. Figure 4.18 presents a schematic of the test setup. And figure 4.19 presents the test setup for the junction temperature mapping experiments.

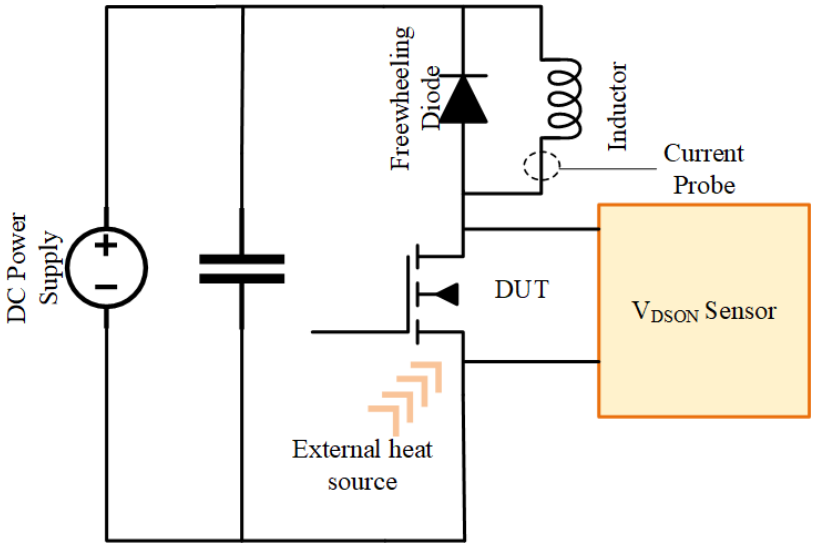

Figure 4.18: Schematics of circuit for junction temperature mapping.

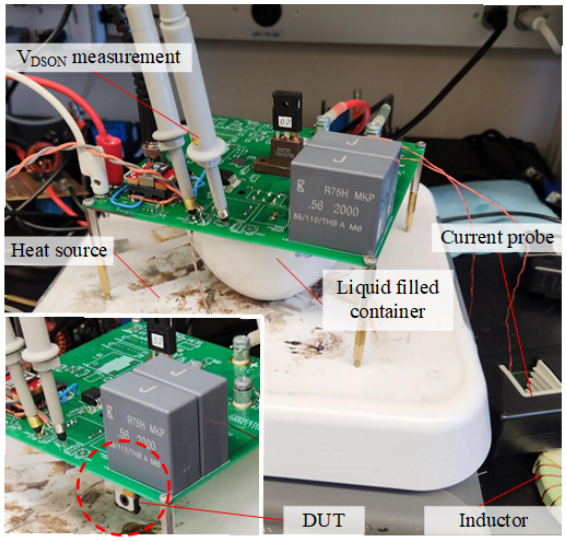

Figure 4.19: Experiment setup for the junction temperature mapping.

A TO247 SiC MOSFET [70] has been used for the junction temperature mapping experiment. The MOSFET is heated with an external heat source at a slow speed so that the MOSFET case and junction temperatures are close. For a homogenous distribution of the heat into the MOSFET, it is dipped into a non-conducting liquid, and heat is applied to the liquid with an external heat source. The device is heated to 140°C; the external heat source is turned off. Without any external heat source,

the MOSFET and the liquid cool naturally. T_j characterization test is run during the natural cooling of the device.

To ensure homogenous heating and prevent hotspots, the DUT was dipped in a bowl of electrically non-conductive oil and applied slowly. Figure 4.20 shows that it took more than three hours to raise the temperature from 30°C to 95°C. This is a really slow temperature rise. The slow temperature rise rate is caused by using a ceramic bowl that does not conduct heat well. The rate of temperature rise could be increased a little bit without creating hotspots. The temperature of the liquid is measured using a fluke thermocouple thermometer, and the temperature data is transmitted to a cell phone from the fluke thermometer for reference.

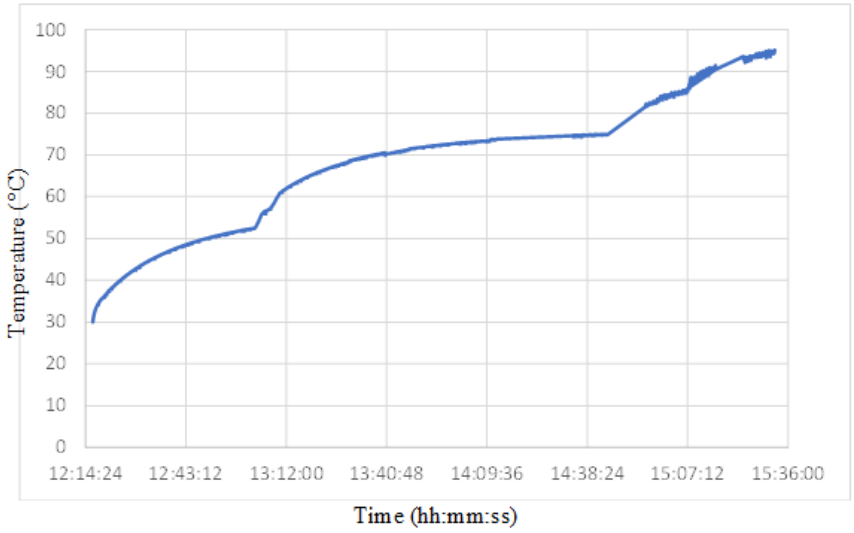

Figure 4.20: Example of recorded temperature during the heating of the DUT.

During the natural cooling, a single pulse of inductive ramp current for $220\mu s$ is run through the DUT at certain temperature intervals. The MOSFET's case temperature, V_{DSON}, and current are captured during every pulse. Figure 4.21 presents such a capture from the oscilloscope.

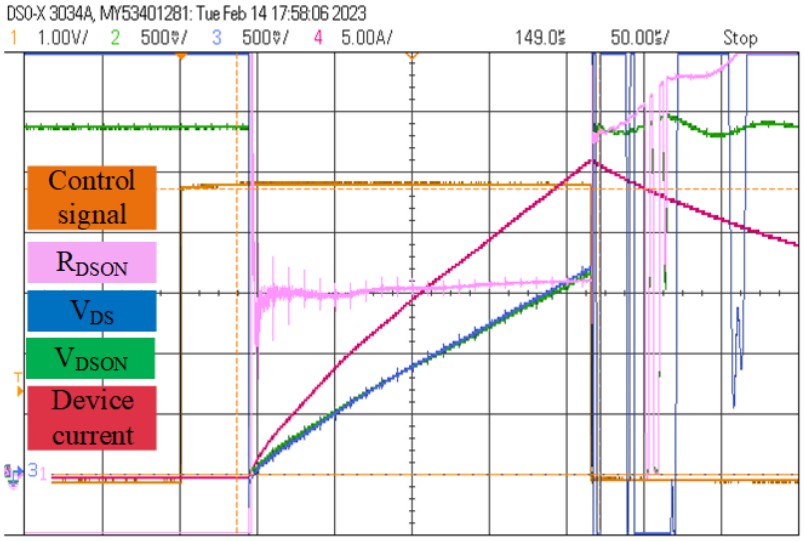

Figure 4.21: Oscilloscope capture for the junction temperature mapping experiment at 40 C.

The internal heat generated is negligible as the current is applied only for a single pulse of $220\mu s$. For a ramp current ramping from 0A to 25A, the power loss in the device is $0.5 \times (I_1^2 + I_1^2) \times R = 0.5 \times 25^2 \times 0.1 = 31.25$ watts. Considering a $100m\Omega$ R_{DSON} of the MOSFET. According to the datasheet [70] of the MOSFET for a $220\mu s$ single pulse, the junction to case thermal impedance is less than $0.07°C/W$. Therefore maximum junction temperature rise in a single pulse will be less than $31.25 \times 0.07 = 2.1875°C$.

From the test V_{DSON} and I_{DS} waveforms, V_{DSON} is sampled at 1A current increment up to 25A for each temperature interval. Figure 4.22 presents a plot of the V_{DSON} vs. I_{DS} samples at temperatures from $40°C$ to $140°C$.

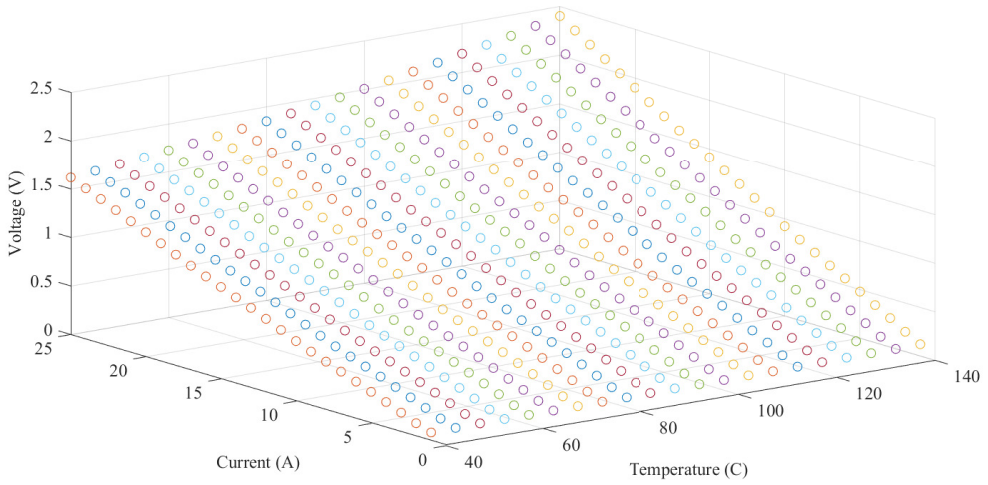

Figure 4.22: Experiment results of junction temperature vs. V_{DSON} vs. I_{DS} samples.

From the sampled V_{DSON} and I_{DS} data, R_{DSON} is calculated for each sample point for junction temperature $40°C$ to $140°C$. A plot of current vs. R_{DSON} at different junction temperatures is presented in figure 4.23. The DUT used in this experiment [70] has $80to144m\Omega$ R_{DSON} listed on the datasheet for a 20A drain current. The experimental results shows R_{DSON} measurements ranging from $64 - 95m\Omega$ R_{DSON} under similar conditon. Which is within the datasheet provided range.

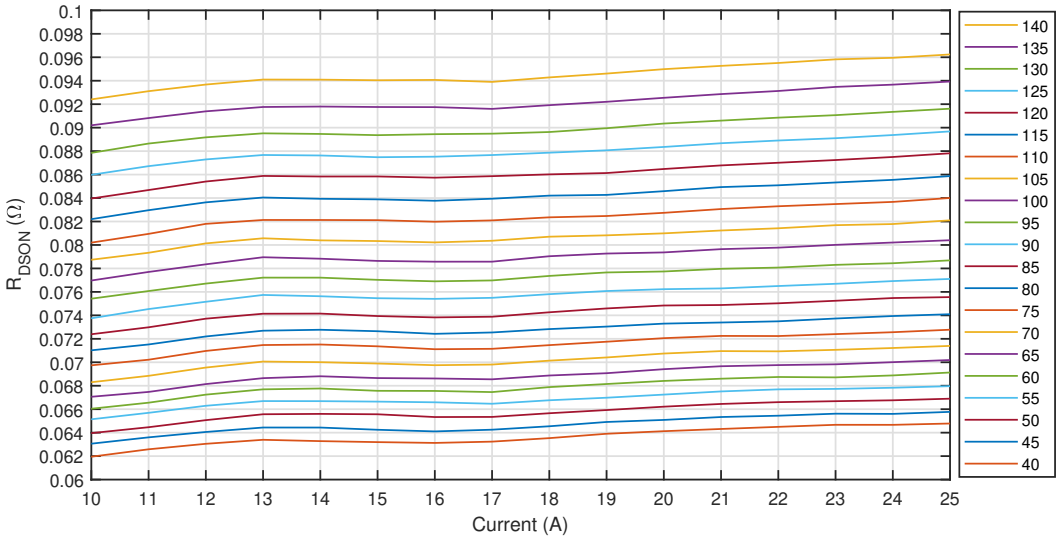

Figure 4.23: Experiment results of drain current vs. R_{DSON} at different junction temperature.

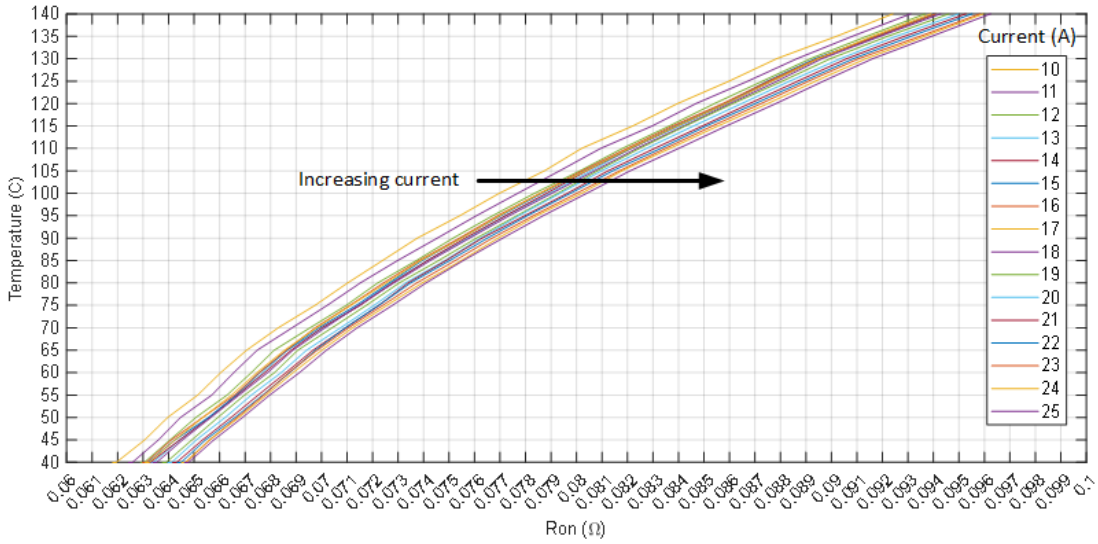

Figure 4.24: Experiment results of R_{DSON} vs. junction temperature at different currents.

During real-time operation, the junction temperature can be estimated by implementing either a look-up table or a simplified equation derived from the R_{DSON}, vs. I_{DS}, vs T_j mapping. Figure 4.24 presents a plot of the junction temperature vs. R_{DSON} for current ranging from 10A to 25A. This data can be used as a reference for the real-time junction temperature calculation. For example, during converter operation, if $86m\Omega$ R_{DSON} is measured at $10A$ current, then the junction temperature is $125°C$.

The online junction temperature can be used in active control to increase the converter's useful life and it could also be used to determine the device's end-of-life (EOF). In an active control approach, for example, in a system of multiple converters operating in parallel, if one of the MOSFETs T_j reaches the maximum limit of the device's safe operating range, the delivered power from that converter could be shared among other converters to maintain a safe T_j.

For another example, we can consider an electric vehicle charging station. The power delivery of an electric vehicle charging station can be maximized with real-

time T_j information. The charging station can be pushed to the limit until the semiconductor devices' T_j reaches the maximum of the safe operating range. Similarly, the power delivery can be reduced if T_j exceeds the safe operating limit. Thus real-time T_j can help utilize the full potential of a power electronics converter. Figure 4.25 proposes a simplified strategy to determine the end of life of a device based on junction temperature.

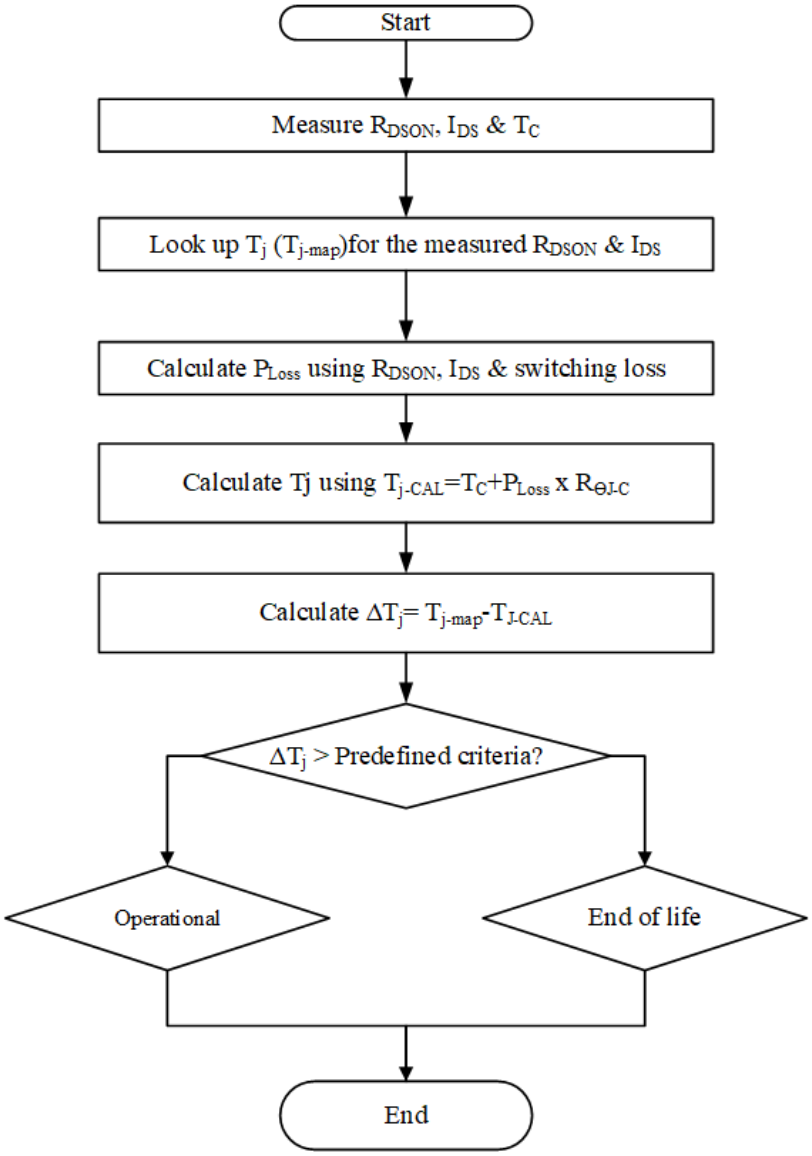

Figure 4.25: Simplified strategy to determine the end of life based on junction temperature.

The more the difference between the online junction temperature estimated from the R_{DSON} vs. T_j mapping and junction temperature calculated from the power loss equation, the more aged the device is. To use the simplified strategy proposed in figure 4.25 the EOF criterion needs to be determined, which is a future research.

CHAPTER 5: CONCLUSIONS AND FUTURE WORK

5.1 Conclusions

In this dissertation, a real-time in-situ health monitoring of a three-phase 1000 VDC to 480 VAC inverter is presented. R_{DSON} is used as the health-monitoring indicator and a process of obtaining R_{DSON} vs. T_j mapping is proposed. The use of the real-time R_{DSON} and T_j information in the active control and degradation monitoring is discussed. In the active control approach, the converter can be used with its full capability if T_j is monitored. Online T_j also makes power sharing among parallel converters more efficient and optimized. For the implementation, V_{DSON} sensors have been investigated. Two configurations of online V_{DSON} measurement circuits are presented. Any one of these two configurations can be selected for online in-situ R_{DSON} monitoring of MOSFETs/IGBTs in a DC-DC or DC-AC power electronics converter. Experiment results have been presented validating different circuit components of the sensor and example application provided for both configurations. A complete architecture of an online in-situ R_{DSON} monitoring in a three-phase DC-AC inverter was presented. The design challenges were identified thoroughly including different propagation delays, switching noises, isolator operating range, etc. A software algorithm was proposed and implemented to collect real-time V_{DSON} and I_{DS} data from the inverter operating environment, filter the useful data, calculate and report the in-situ R_{DSON} of the power MOSFETs. Using the proposed sensing circuit and processing algorithm Real-time R_{DSON} of the six MOSFETs are measured under 1000VDC to 480VAC sinusoidal operation at 30kW power and presented in this article. The online in-situ AC R_{DSON} of the six MOSFETs ranges $6.0m\Omega$ to $7.5m\Omega$ which is on average $0.5m\Omega$ higher than the DC (true) R_{DSON}. This increase is due

to parasitic impedances that only affect the AC measurements. A comprehensive AC impedance analysis is presented that supports the observed results. The data can be utilized to assess the degradation and the remaining useful lifetime of the inverter. In addition, a junction temperature mapping with R_{DSON} and I_DS is presented. The mapping can be used for real-time T_j estimation for active control or EOF detection.

5.2 Future works

This article presents sensor design and methods of online in-situ R_{DSON} and T_j monitoring of power MOSFETs and IGBTs. These parameters are directly related to the device's degradation and operational stress. Proper control architectures based on different applications are required along with the sensing solution for the best outcome. Proper active control and a method to quantify device degradation need to be implemented to use the sensing solutions provided in this article to their full potential. Finding a proper quantification strategy for the device degradation and EOF criteria and active control strategies are the future work of this research.

REFERENCES

[1] B. K. Bose, "Global energy scenario and impact of power electronics in 21st century," *IEEE Transactions on Industrial Electronics*, vol. 60, no. 7, pp. 2638–2651, 2012.

[2] N. Kim, C. Roy, R. Cox, and B. Parkhideh, "A plug and play power electronics education board for hands-on learning of power converters incorporating wbg semiconductor," in *2019 10th International Conference on Power Electronics and ECCE Asia (ICPE 2019 - ECCE Asia)*, pp. 2807–2813, 2019.

[3] C. Roy, N. Kim, R. Cox, and B. Parkhideh, "Development of a power electronics teaching lab incorporating wbg semiconductors with plug and play modular hardware and advanced curriculum," in *2019 IEEE Energy Conversion Congress and Exposition (ECCE)*, pp. 2432–2438, 2019.

[4] L. F. Costa and M. Liserre, "Failure analysis of the dc-dc converter: A comprehensive survey of faults and solutions for improving reliability," *IEEE Power Electronics Magazine*, vol. 5, no. 4, pp. 42–51, 2018.

[5] B. Ji, X. Song, W. Cao, V. Pickert, Y. Hu, J. W. Mackersie, and G. Pierce, "In situ diagnostics and prognostics of solder fatigue in igbt modules for electric vehicle drives," *IEEE Transactions on Power Electronics*, vol. 30, no. 3, pp. 1535–1543, 2014.

[6] Y. Peng, S. Zhao, and H. Wang, "A digital twin based estimation method for health indicators of dc–dc converters," *IEEE Transactions on Power Electronics*, vol. 36, no. 2, pp. 2105–2118, 2020.

[7] B. Ji, V. Pickert, W. Cao, and B. Zahawi, "In situ diagnostics and prognostics of wire bonding faults in igbt modules for electric vehicle drives," *IEEE Transactions on Power Electronics*, vol. 28, no. 12, pp. 5568–5577, 2013.

[8] U.-M. Choi, F. Blaabjerg, S. Jørgensen, S. Munk-Nielsen, and B. Rannestad, "Reliability improvement of power converters by means of condition monitoring of igbt modules," *IEEE Transactions on Power Electronics*, vol. 32, no. 10, pp. 7990–7997, 2016.

[9] V. Smet, F. Forest, J.-J. Huselstein, A. Rashed, and F. Richardeau, "Evaluation of vce monitoring as a real-time method to estimate aging of bond wire-igbt modules stressed by power cycling," *IEEE Transactions on Industrial Electronics*, vol. 60, no. 7, pp. 2760–2770, 2012.

[10] A. Griffo, J. Wang, K. Colombage, and T. Kamel, "Real-time measurement of temperature sensitive electrical parameters in sic power mosfets," *IEEE Transactions on Industrial Electronics*, vol. 65, no. 3, pp. 2663–2671, 2017.

[11] A. Singh, A. Anurag, and S. Anand, "Evaluation of vce at inflection point for monitoring bond wire degradation in discrete packaged igbts," *IEEE Transactions on Power Electronics*, vol. 32, no. 4, pp. 2481–2484, 2016.

[12] E. Ugur, C. Xu, F. Yang, S. Pu, and B. Akin, "A new complete condition monitoring method for sic power mosfets," *IEEE Transactions on Industrial Electronics*, vol. 68, no. 2, pp. 1654–1664, 2020.

[13] M. Guacci, D. Bortis, and J. W. Kolar, "On-state voltage measurement of fast switching power semiconductors," *CPSS Transactions on Power Electronics and Applications*, vol. 3, no. 2, pp. 163–176, 2018.

[14] S. Pu, F. Yang, B. T. Vankayalapati, E. Ugur, C. Xu, and B. Akin, "A practical on-board sic mosfet condition monitoring technique for aging detection," *IEEE Transactions on Industry Applications*, vol. 56, no. 3, pp. 2828–2839, 2020.

[15] S. Dusmez, M. Heydarzadeh, M. Nourani, and B. Akin, "Remaining useful lifetime estimation for power mosfets under thermal stress with ransac outlier removal," *IEEE Transactions on Industrial Informatics*, vol. 13, no. 3, pp. 1271–1279, 2017.

[16] S. Zhao, Y. Peng, F. Yang, E. Ugur, B. Akin, and H. Wang, "Health state estimation and remaining useful life prediction of power devices subject to noisy and aperiodic condition monitoring," *IEEE Transactions on Instrumentation and Measurement*, vol. 70, pp. 1–16, 2021.

[17] F. Gonzalez-Hernando, J. San-Sebastian, A. Garcia-Bediaga, M. Arias, F. Iannuzzo, and F. Blaabjerg, "Wear-out condition monitoring of igbt and mosfet power modules in inverter operation," *IEEE Transactions on Industry Applications*, vol. 55, no. 6, pp. 6184–6192, 2019.

[18] Y. Peng and H. Wang, "A simplified on-state voltage measurement circuit for power semiconductor devices," *IEEE Transactions on Power Electronics*, vol. 36, no. 10, pp. 10993–10997, 2021.

[19] M. A. Eleffendi and C. M. Johnson, "Evaluation of on-state voltage v ce (on) and threshold voltage v th for real-time health monitoring of igbt power modules," in *2015 17th European Conference on Power Electronics and Applications (EPE'15 ECCE-Europe)*, pp. 1–10, IEEE, 2015.

[20] X. Wang, P. Sun, L. Sun, Q. Luo, and X. Du, "Online condition monitoring for bond wire degradation of igbt modules in three-level neutral-point-clamped converters," *IEEE Transactions on Industrial Electronics*, vol. 68, no. 8, pp. 7474–7484, 2020.

[21] M. Ma, B. Ji, J. Han, J. Wang, M. Zhan, and N. Xiang, "In-situ health monitoring of igbt modules of an on-line medium-voltage inverter system using industrial internet of things," *CSEE Journal of Power and Energy Systems*, vol. 6, no. 3, pp. 638–648, 2020.

[22] F. Gonzalez-Hernando, J. San-Sebastian, M. Arias, A. Rujas, and F. Iannuzzo, "Discontinuous pwm for online condition monitoring of sic power modules," *IEEE Journal of Emerging and Selected Topics in Power Electronics*, vol. 8, no. 1, pp. 323–330, 2019.

[23] L. Rossetto and G. Spiazzi, "A fast on-state voltage measurement circuit for power devices characterization," *IEEE Transactions on Power Electronics*, vol. 37, no. 5, pp. 4926–4930, 2021.

[24] D. Mingxing, W. Kexin, L. Jian, and X. Linlin, "Condition monitoring igbt module bond wire lift-off using measurable signals," in *Proceedings of the 7th international power electronics and motion control conference*, vol. 2, pp. 1492–1496, IEEE, 2012.

[25] B. Ji, V. Pickert, and B. Zahawi, "In-situ bond wire and solder layer health monitoring circuit for igbt power modules," in *2012 7th International Conference on Integrated Power Electronics Systems (CIPS)*, pp. 1–6, IEEE, 2012.

[26] B. Ji, V. Pickert, W. P. Cao, and L. Xing, "Onboard condition monitoring of solder fatigue in igbt power modules," in *2013 9th IEEE International Symposium on Diagnostics for Electric Machines, Power Electronics and Drives (SDEMPED)*, pp. 9–15, 2013.

[27] D. Wagenitz, A. Hambrecht, and S. Dieckerhoff, "Lifetime evaluation of igbt power modules applying a nonlinear saturation voltage observer," in *2012 7th International Conference on Integrated Power Electronics Systems (CIPS)*, pp. 1–5, 2012.

[28] B. Ji, V. Pickert, B. Zahawi, and M. Zhang, "In-situ bond wire health monitoring circuit for igbt power modules," in *6th IET International Conference on Power Electronics, Machines and Drives (PEMD 2012)*, pp. 1–6, 2012.

[29] Y. Peng, Y. Shen, and H. Wang, "A condition monitoring method for three phase inverter based on system-level signal," in *2018 IEEE International Power Electronics and Application Conference and Exposition (PEAC)*, pp. 1–5, 2018.

[30] J. Wei, S. Liu, J. Fang, S. Li, T. Li, and W. Sun, "Investigation on degradation mechanism and optimization for sic power mosfets under long-term short-circuit stress," in *2018 IEEE 30th International Symposium on Power Semiconductor Devices and ICs (ISPSD)*, pp. 399–402, IEEE, 2018.

[31] X. Yang, Y. Chen, B. Hou, X. Xu, J. Wang, Y. Huang, Q. Chen, and C. Zhou, "Degradation behavior and defect analysis for sic power mosfets based on low-frequency noise under repetitive power-cycling stress," *IEEE Transactions on Electron Devices*, vol. 68, no. 2, pp. 666–671, 2020.

[32] J. Morroni, A. Dolgov, M. Shirazi, R. Zane, and D. Maksimovic, "Online health monitoring in digitally controlled power converters," in *2007 IEEE Power Electronics Specialists Conference*, pp. 112–118, IEEE, 2007.

[33] H. Chen, B. Ji, V. Pickert, and W. Cao, "Real-time temperature estimation for power mosfets considering thermal aging effects," *IEEE Transactions on Device and Materials Reliability*, vol. 14, no. 1, pp. 220–228, 2013.

[34] S. H. Ali, E. Ugur, and B. Akin, "Analysis of vth variations in igbts under thermal stress for improved condition monitoring in automotive power conversion systems," *IEEE Transactions on Vehicular Technology*, vol. 68, no. 1, pp. 193–202, 2019.

[35] L. Ren, Q. Shen, and C. Gong, "Real-time aging monitoring for power mosfets using threshold voltage," in *IECON 2016 - 42nd Annual Conference of the IEEE Industrial Electronics Society*, pp. 441–446, 2016.

[36] X. Ye, C. Chen, Y. Wang, G. Zhai, and G. J. Vachtsevanos, "Online condition monitoring of power mosfet gate oxide degradation based on miller platform voltage," *IEEE Transactions on Power Electronics*, vol. 32, no. 6, pp. 4776–4784, 2016.

[37] J. Liu, G. Zhang, Q. Chen, L. Qi, Y. Geng, and J. Wang, "In situ condition monitoring of igbts based on the miller plateau duration," *IEEE Transactions on Power Electronics*, vol. 34, no. 1, pp. 769–782, 2018.

[38] S. Zhou, L. Zhou, and P. Sun, "Monitoring potential defects in an igbt module based on dynamic changes of the gate current," *IEEE Transactions on Power Electronics*, vol. 28, no. 3, pp. 1479–1487, 2012.

[39] F. Erturk and B. Akin, "A method for online ageing detection in sic mosfets," in *2017 IEEE Applied Power Electronics Conference and Exposition (APEC)*, pp. 3576–3581, IEEE, 2017.

[40] K. Wang, L. Zhou, P. Sun, and X. Du, "Monitoring bond wires fatigue of multichip igbt module using time duration of the gate charge," *IEEE Transactions on Power Electronics*, vol. 36, no. 1, pp. 888–897, 2020.

[41] A. Hanif, S. Das, and F. Khan, "Active power cycling and condition monitoring of igbt power modules using reflectometry," in *2018 IEEE Applied Power Electronics Conference and Exposition (APEC)*, pp. 2827–2833, IEEE, 2018.

[42] Z. Wang, B. Tian, W. Qiao, and L. Qu, "Real-time aging monitoring for igbt modules using case temperature," *IEEE Transactions on Industrial Electronics*, vol. 63, no. 2, pp. 1168–1178, 2015.

[43] J. Zhang, X. Du, Y. Yu, S. Zheng, P. Sun, and H.-M. Tai, "Thermal parameter monitoring of igbt module using junction temperature cooling curves," *IEEE Transactions on Industrial Electronics*, vol. 66, no. 10, pp. 8148–8160, 2018.

[44] A. Brunko, W. Holzke, H. Groke, B. Orlik, and N. Kaminski, "Model-based condition monitoring of power semiconductor devices in wind turbines," in *2019 21st*

European Conference on Power Electronics and Applications (EPE '19 ECCE Europe), pp. P.1–P.9, 2019.

[45] J. Naghibi, K. Mehran, and M. P. Foster, "An online failure assessment approach for sic-based mosfet power modules using iterative condition monitoring technique," in *2020 IEEE 21st Workshop on Control and Modeling for Power Electronics (COMPEL)*, pp. 1–5, 2020.

[46] B. Tian, W. Qiao, Z. Wang, T. Gachovska, and J. L. Hudgins, "Monitoring igbt's health condition via junction temperature variations," in *2014 IEEE Applied Power Electronics Conference and Exposition - APEC 2014*, pp. 2550–2555, 2014.

[47] P. Sun, C. Gong, X. Du, Y. Peng, B. Wang, and L. Zhou, "Condition monitoring igbt module bond wires fatigue using short-circuit current identification," *IEEE Transactions on Power Electronics*, vol. 32, no. 5, pp. 3777–3786, 2016.

[48] P. Sun, C. Gong, X. Du, Q. Luo, H. Wang, and L. Zhou, "Online condition monitoring for both igbt module and dc-link capacitor of power converter based on short-circuit current simultaneously," *IEEE Transactions on Industrial Electronics*, vol. 64, no. 5, pp. 3662–3671, 2017.

[49] S. Pu, E. Ugur, F. Yang, and B. Akin, "In situ degradation monitoring of sic mosfet based on switching transient measurement," *IEEE Transactions on Industrial Electronics*, vol. 67, no. 6, pp. 5092–5100, 2019.

[50] P. Sun, Y. Guo, T. Wu, Z. Zhao, P. Lai, Z. Chen, L. Qi, and X. Cui, "An online junction temperature monitoring correction method for sic mosfets at different parasitic parameters," *IEEE Journal of Emerging and Selected Topics in Power Electronics*, vol. 10, no. 5, pp. 5007–5018, 2022.

[51] J. Naghibi, S. Mohsenzade, K. Mehran, and M. P. Foster, "Gate oxide degradation condition monitoring technique for high-frequency applications of silicon carbide power mosfets," *IEEE Transactions on Power Electronics*, vol. 38, no. 1, pp. 1079–1091, 2023.

[52] J. O. Gonzalez, O. Alatise, J. Hu, L. Ran, and P. Mawby, "Temperature sensitive electrical parameters for condition monitoring in sic power mosfets," in *8th IET International Conference on Power Electronics, Machines and Drives (PEMD 2016)*, pp. 1–6, 2016.

[53] L. Qiao, F. Wang, J. Dyer, and Z. Zhang, "Online junction temperature monitoring for sic mosfets using turn-on delay time," in *2020 IEEE Applied Power Electronics Conference and Exposition (APEC)*, pp. 1526–1531, 2020.

[54] E. Aeloiza, A. Kadavelugu, L. Liu, and J. Puukko, "Online health monitoring and aging prognostics for sic power converters," in *2020 IEEE Energy Conversion Congress and Exposition (ECCE)*, pp. 670–676, 2020.

[55] J. Henn, C. Lüdecke, M. Laumen, S. Beushausen, S. Kalker, C. H. van der Broeck, G. Engelmann, and R. W. de Doncker, "Intelligent gate drivers for future power converters," *IEEE Transactions on Power Electronics*, vol. 37, no. 3, pp. 3484–3503, 2021.

[56] K. Li, G. Y. Tian, L. Cheng, A. Yin, W. Cao, and S. Crichton, "State detection of bond wires in igbt modules using eddy current pulsed thermography," *IEEE Transactions on Power Electronics*, vol. 29, no. 9, pp. 5000–5009, 2013.

[57] C. H. van der Broeck, R. D. Lorenz, and R. W. De Doncker, "Monitoring 3-d temperature distributions and device losses in power electronic modules," *IEEE Transactions on Power Electronics*, vol. 34, no. 8, pp. 7983–7995, 2018.

[58] C. H. van der Broeck, T. A. Polom, R. D. Lorenz, and R. W. De Doncker, "Real-time monitoring of thermal response and life-time varying parameters in power modules," *IEEE Transactions on Industry Applications*, vol. 56, no. 5, pp. 5279–5291, 2020.

[59] Z. Zhang, C. Chen, A. Suetake, H. Ishino, H. Sampei, T. Endo, K. Sugiura, K. Tsuruta, and K. Suganuma, "Online condition monitoring of solder fatigue in a clip-bonding sic mosfet power assembly via acoustic emission technique," *IEEE Transactions on Power Electronics*, vol. 38, no. 2, pp. 1468–1478, 2023.

[60] A. Hanif, D. DeVoto, and F. Khan, "Bond wire damage detection and soh estimation of a dual-pack igbt power module using active power cycling and reflectometry," *IEEE Transactions on Power Electronics*, vol. 35, no. 7, pp. 6761–6772, 2019.

[61] M. Andresen, M. Liserre, and G. Buticchi, "Review of active thermal and life-time control techniques for power electronic modules," in *2014 16th European Conference on Power Electronics and Applications*, pp. 1–10, 2014.

[62] M. Andresen, J. Kuprat, V. Raveendran, J. Falck, and M. Liserre, "Active thermal control for delaying maintenance of power electronics converters," *Chinese Journal of Electrical Engineering*, vol. 4, no. 3, pp. 13–20, 2018.

[63] N. Baker, M. Liserre, L. Dupont, and Y. Avenas, "Junction temperature measurements via thermo-sensitive electrical parameters and their application to condition monitoring and active thermal control of power converters," in *IECON 2013 - 39th Annual Conference of the IEEE Industrial Electronics Society*, pp. 942–948, 2013.

[64] N. Badawi and S. Dieckerhoff, "A new method for dynamic ron extraction of gan power hemts," in *Proceedings of PCIM Europe 2015; International Exhibition and Conference for Power Electronics, Intelligent Motion, Renewable Energy and Energy Management*, pp. 1–6, VDE, 2015.

[65] C. Roy and B. Parkhideh, "Design consideration for characterization and study of dynamic on state resistance of gan devices," in *2019 IEEE 7th Workshop on Wide Bandgap Power Devices and Applications (WiPDA)*, pp. 181–186, IEEE, 2019.

[66] C. Roy, N. Kim, J. Gafford, and B. Parkhideh, "On-state voltage measurement of high-side power transistors in three-phase four-leg inverter for in-situ prognostics," in *2021 IEEE Energy Conversion Congress and Exposition (ECCE)*, pp. 2770–2776, 2021.

[67] Cree Inc., CAS300M17BM2 datasheet, *1.7kV, 8.0 mΩ All-Silicon Carbide Half-Bridge Module*, Jan 2020.

[68] C. Roy, N. Kim, D. Evans, A. P. Sirat, J. Gafford, and B. Parkhideh, "A half-bridge on-state voltage sensor for in-situ measurements," in *2022 IEEE Energy Conversion Congress and Exposition (ECCE)*, pp. 1–7, 2022.

[69] Cree Inc., CAS300M12BM2 datasheet, *1200 V, 300 A All-Silicon Carbide High Performance, Switching Optimized, Half-Bridge Module*, Jan 2021.

[70] Cree Inc., C2M0080120D datasheet, *Silicon Carbide Power MOSFET C2MTM MOSFET Technology N-Channel Enhancement*, Jan 2023.